Geosci. Model Dev. Discuss., doi:10.5194/gmd-2016-53, 2016
Manuscript under review for journal Geosci. Model Dev.
Published: 17 May 2016

Geoscientific Model Development Discussions

A Joint Global Carbon Inversion System Using Both CO_2 and CO_2 Atmospheric Concentration Data

Jing M. Chen1,2, Gang Mo1, Feng Deng1

[1]Department of Geography and Program in Planning, University of Toronto, 100 St. George Street
Toronto, Ontario, Canada M5S 3G3
[2]International Institute of Earth System Science, Nanjing University, 22 Hankou Road, Nanjing, Jiangsu, China, 210093

Corresponding author: Jing M. Chen (chenj@geog.utoronto.ca)

Abstract. Observations of 13CO2 at 73 sites compiled in the GLOBALVIEW database are used for an additional constraint in a global atmospheric inversion of the surface CO2 flux using CO2 observations at 210 sites (62 collocated with 13CO2 sites) for the 2002-2004 period for 39 land regions and 11 ocean regions. This constraint is implemented using prior CO2 fluxes estimated with a terrestrial ecosystem model and an ocean model. These models simulate 13CO2 discrimination rates of terrestrial photosynthesis and ocean-atmosphere diffusion processes. In both models, the 13CO2 disequilibrium between fluxes to and from the atmosphere is considered due to the historical change in atmospheric 13CO2 concentration. This joint inversion system using both13CO2 and CO2 observations is effectively a double deconvolution system with consideration of the spatial variations of isotopic discrimination and disequilibrium. This 13CO2 constraint on the inversion considerably reduces the total land carbon sink from 3.40±0.84 to 2.78±0.76 Pg C y-1 but increases the total oceanic carbon sink from 1.48±0.40 to 2.26 ±0.35 Pg C y-1. This constraint also changes the spatial distribution of the carbon sink. The largest sink increase occurs in Amazon, while the largest source increases are in southern Africa, and Asia, where CO2 data are sparse. Through a case study, in which the spatial distribution of the annual 13CO2 discrimination rate over land is ignored by treating it as a constant at the global average of -14.1‰, the spatial distribution of the inverted CO2 flux over land was found to be significantly modified (up to 15% for some regions). The uncertainties in our disequilibrium flux estimation are 11.2 PgC y-1 ‰ and 16.3 Pg C y-1 ‰ for land and ocean, respectively. These uncertainties induced uncertainties of 0.47 Pg C y-1 and 0.54 Pg C y-1 in the inverted CO2 fluxes for land and ocean, respectively. Our joint inversion system is therefore useful for improving the partitioning between ocean and land sinks and the spatial distribution of the inverted carbon flux.

Keywords: ^{13}C isotope, atmospheric inversion, carbon cycle, ecosystem modelling

1. Introduction

Over the last few decades, much progress has been made in estimating the global carbon cycle using different methods (*Houghton et al.*, 2007; *Canadell et al.*, 2007; *Le Quéré et al.*, 2013). In particular, atmospheric CO_2 mole fractions measured near the surface have been used to infer the carbon flux over land and ocean surfaces through atmospheric

Geosci. Model Dev. Discuss., doi:10.5194/gmd-2016-53, 2016
Manuscript under review for journal Geosci. Model Dev.
Published: 17 May 2016

Geoscientific Model Development Discussions

inversion (*Rödenbeck et al*., 2003; *Michalak et al*., 2005; *Peylin et al*., 2005; *Peters et al*., 2007). However, the uncertainty in the inferred flux is still very large, mostly because of the insufficient number of observation stations and the error in modeling the atmospheric transport of CO_2 from the surface to the observation stations. To reduce this uncertainty, it would be useful to introduce constraints to the inversion using other gas species that are associated the CO_2 flux.

Measurements of the atmospheric concentration of the stable isotope $^{13}CO_2$ at a number of stations across the globe since 1994 have been compiled in a database (*GLOBALVIEW-CO2C13*, 2009), and the number of extended $^{13}CO_2$ records from January 1994 to January 2009 increased to 76 by 2009. The mole fraction of $^{13}CO_2$ to CO_2 in the atmosphere is about 1.1%, and the CO_2 exchange between the surface and the atmosphere generally induces concurrent $^{13}CO_2$ exchange. However, the proportion of the $^{13}CO_2$ flux relative to the CO_2 flux differs at different locations and different times due to different mechanisms that discriminate against heavier $^{13}CO_2$ molecules in the exchange processes, and therefore the $^{13}CO_2$ concentration measured in the atmosphere contains additional information for the CO_2 flux. This information is useful for differentiating between terrestrial and oceanic CO_2 exchanges with the atmosphere because the terrestrial CO_2 flux experiences much greater discrimination against $^{13}CO_2$ than does the oceanic CO_2 flux (*Tans et al*., 1990; *Ciais et al*., 1995a; *Francey et al*., 1995). Observed $^{13}CO_2$ mole fractions can also provide independent information on the net CO_2 exchange over land and ocean because the net carbon flux to the surface discriminates against heavier $^{13}CO_2$ (*Fung et al*., 1997; *Randerson et al*., 2002; *Suits et al*., 2005). The $^{13}CO_2$ observations over the globe, albeit with a limited number of stations, could therefore be used to assist in quantifying the global carbon cycle.

In previous studies (*Siegenthaler and Oeschger*, 1987; *Keeling et al*., 1989a; *Francey et al*., 1995; *Randerson et al*., 2002), atmospheric $^{13}CO_2$ observations have been used to separate ocean and land CO_2 fluxes through the use of a technique dubbed "double deconvolution", by which the CO_2 fluxes of land and ocean are separated (deconvolved) based on different discrimination rates against $^{13}CO_2$ in the atmospheric CO_2 exchange with land and ocean surfaces. This double deconvolution often assumes that the discrimination rates over land and ocean are spatially uniform, although they can be temporally variable. Through forward atmospheric transport modeling, the ocean and land CO_2 fluxes were also separated based on the spatial gradients of the measured $^{13}CO_2/CO_2$ ratio either globally (*Keeling et al*., 1989b) or by latitudinal bands (*Ciais et al*., 1995a). The same $^{13}CO_2$ data have also been used in inverse modeling of the surface CO_2 flux (*Enting et al*., 1995; *Rayner et al*., 1999; *Rayner et al*., 2008). *Enting et al*. (1995) pioneered a methodology for inverting annual mean ocean and land CO_2 fluxes from both atmospheric CO_2 and $^{13}CO_2$ concentration data for 12 ocean regions and 8 land ecosystems for the 1986-1987 and 1989-1990 periods. *Rayner et al*. (1999) developed a different methodology to invert monthly CO_2 fluxes for 12 ocean and 14 land regions for the period from 1980 to 1995 from CO_2 observations at 12 stations and $^{13}CO_2$ and O_2/N_2 observations at 1 station. *Rayner et al*. (2008) refined their methodology and applied it to the period from 1992 to 2005 using CO_2 at 67 sites and $^{13}CO_2$ at 10 sites. These studies showed the usefulness of the additional information from $^{13}CO_2$ observations in improving the inversion of annual mean and seasonality of the CO_2 flux over land and ocean. In these inversion studies, the discrimination rate for land is either assumed to be a constant (*Enting et al*., 1995; *Rayner et al*., 1999) or allowed to vary with the areal fraction of C4 plant in a region (*Rayner et al*., 2008). These inversions based on the

Geosci. Model Dev. Discuss., doi:10.5194/gmd-2016-53, 2016
Manuscript under review for journal Geosci. Model Dev.
Published: 17 May 2016

Geoscientific Model Development Discussions

Bayesian principle were also constrained with only simple prior estimates of the terrestrial and oceanic CO_2 and $^{13}CO_2$ fluxes. Since the data density (the numbers of CO_2 and $^{13}CO_2$ observation sites) is low, the assumed discrimination constants and these prior estimates would have considerable influence on the inverted results, as this is clearly demonstrated in *Enting et al*. (1995).

Atmospheric CO_2 observations have been extensively used to estimate the carbon flux over ocean and land through inverse modeling using Bayesian synthesis (*Gurnay et al.,* 2002*; Rödenbeck et al.,*2003*; Baker et al.,* 2006*; Peylin et al.* 2005) or data assimilation techniques (*Peters et al.,* 2007; *Zhang et al.*, 2014). Atmospheric inversion studies (*Gurnay et al.*, 2003; *Jacobson et al.,* 2007) often produced ocean sinks considerably smaller than those estimated based on observed gradients in dissolved inorganic carbon (DIC) in interior ocean using ocean circulation models (*Steinkamp and Gruber*, 2013). Recent estimates for the ocean sink for anthropogenic CO_2 in 2000's based on DIC ranges from 1.6 to 2.6 Pg C y^{-1} (*Park et al*., 2010; *Wanninkhof et al*., 2013; *Landschützer et al.*, 2014; *Majkut et al.*, 2014; *DeVries*, 2014; *Rödenbeck et al.*, 2014) with an uncertainty of about 0.6 Pg C y^{-1}, while atmospheric inversion results are not yet reliable enough to be included in a global ocean sink synthesis (*Le Quéré et al*., 2013). The partition between ocean and land fluxes using atmospheric inversion techniques is sensitive to errors in atmospheric transport modeling (*Baker et al.*, 2006*; Stephens et al.*, 2007) and prior fluxes for land and ocean used to constrain the inversion (*Zhang et al., 2014; Chen et al.,* 2015). It would therefore be highly desirable to use $^{13}CO_2$ observations to constrain this partition in the inversion process. Accurate partition between ocean and land sinks is important in global carbon cycle research because (1) land sinks are still more reliably estimated as the residual of the global carbon budget than those from land-based data (*Le Quéré et al*., 2013) and (2) ocean sink estimates based on DIC in ocean water also suffer from considerable errors due to insufficient DIC observations and in ocean circulation modeling (*DeVries*, 2014).

The overall goal of this study is to explore the information content of $^{13}CO_2$ measurements for global CO_2 flux estimation through developing a Bayesian synthesis inversion system that uses both CO_2 and $^{13}CO_2$ observations. This system is effectively a new double de-convolution system with the capacity to consider the spatial variations of the prior carbon flux and all major isotopic parameters including photosynthetic discrimination, respiratory signature, and disequilibrium rate. In this study, this new system is used to achieve the following objectives: (1) to partition between ocean and land sinks with consideration of the spatial distributions of $^{13}CO_2$ isotopic parameters over ocean and land; (2) to evaluate the importance of considering the spatial distributions of the $^{13}CO_2$ discrimination rate over land in the inversion of the CO_2 flux, and (3) to assess the impacts of the errors in disequilibrium flux estimation on the flux partition between ocean and land. To achieve these objectives, a terrestrial ecosystem model named the Boreal Ecosystem Productivity Simulator (BEPS) is further developed to simulate the spatial distributions of the $^{13}CO_2$ discrimination and disequilibrium rates over land for use in a global Bayesian synthesis inversion with $^{13}CO_2$ constraint. BEPS is also used to produce CO_2 prior fluxes globally to regularize the inversion.

Geosci. Model Dev. Discuss., doi:10.5194/gmd-2016-53, 2016
Manuscript under review for journal Geosci. Model Dev.
Published: 17 May 2016

2. Methodology

2.1 The inversion method

2.1.1 Inversion system

The nested inversion system with a focus on North America developed by *Deng et al*. (2007) is adopted in this study. In this system, two of the Transcom regions (*Gurney et al*., 2002) in North America are divided into 30 regions according to ecosystem types and administrative boundaries (Figure 1), in order to reduce spatial aggregation errors in the inversion over North America and to investigate the inverted spatial distribution of the carbon flux against ecosystem model results. This nested region serves the purpose of evaluating the influence of the spatial distribution of isotopic discrimination on the inverted carbon flux at a relatively high resolution. Also shown in Figure 1 are the spatial distributions of 210 CO_2 and 73 $^{13}CO_2$ observation sites selected in this study from the NOAA GLOBALVIEW database. Most $^{13}CO_2$ sites except 11 are collocated with CO_2 sites.

2.1.2 Synthesis Bayesian inversion with CO_2 observations

To estimate the CO_2 flux (**f**), we represent the relationship between CO_2 measurements and the flux from the surface by a linear model:

$$\mathbf{c} = \mathbf{G}\mathbf{f} + \mathbf{A}c_0 + \boldsymbol{\varepsilon} \quad (1)$$

where $\mathbf{c}_{m\times1}$ is a given vector of m CO_2 concentration observations over space and time (m equals number of stations times number of months, and for CO_2 only inversion, it is 12600, i.e. 210 stations × 60 months); $\boldsymbol{\varepsilon}_{m\times1}$ is a random error vector with a zero mean and a covariance matrix $\mathrm{cov}(\boldsymbol{\varepsilon}) = \mathbf{R}_{m\times m}$; $\mathbf{G}_{m\times(n-1)}$ is a matrix representing a transport (observation) operator, where n-1 is the number of fluxes to be determined (equals 3000, i.e. 50 regions × 60 months); $\mathbf{A}_{m\times1}$ is a unity vector (filled with 1) representing the assumed initial well-mixed atmospheric CO_2 concentrations (c_0) before the first month; and $\mathbf{f}_{(n-1)\times1}$ is an unknown vector of monthly carbon fluxes of the 50 regions.

Combining matrixes $\mathbf{G}$ and $\mathbf{A}$ as $\mathbf{M}_{m\times n} = (\mathbf{G}, \mathbf{A})$ and vectors $\mathbf{f}$ and c_0 as $\mathbf{s}_{n\times1} = (\mathbf{f}^{\mathbf{T}}, c_0)^{\mathbf{T}}$, eq. (1) can be expressed as

$$\mathbf{c} = \mathbf{M}\mathbf{s} + \boldsymbol{\varepsilon} \quad (2)$$

The inverse problem of estimating **s** from **c** is often poorly constrained and a Bayesian approach is used to circumvent this problem. Pre-existing knowledge and models incorporating additional sources of information can be used to provide an initial estimate of **s**, known as the *a priori*, to constrain the inversion. This *a priori* is then updated when it is

Geosci. Model Dev. Discuss., doi:10.5194/gmd-2016-53, 2016
Manuscript under review for journal Geosci. Model Dev.
Published: 17 May 2016

combined with information from **c** measurement to form a posterior estimate of **s**, known as the *a posteriori*. In Bayesian synthesis inversion (*Tarantola*, 1987), the following objective function is employed in the place of the traditional least square objective function:

$$J = \frac{1}{2}(\mathbf{Ms}-\mathbf{c})^{\mathrm{T}}\mathbf{R}^{-1}(\mathbf{Ms}-\mathbf{c}) + \frac{1}{2}(\mathbf{s}-\mathbf{s_p})^{\mathrm{T}}\mathbf{Q}^{-1}(\mathbf{s}-\mathbf{s_p}) \quad (3)$$

where $\mathbf{s}_{pn\times1}$ is the *a priori* estimate of $\mathbf{s}$; the covariance matrix $\mathbf{Q}_{n\times n}$ represents the uncertainty in the *a priori* estimate; and $\mathbf{R}_{m\times m}$ is the transport model-data mismatch error covariance. By minimizing this objective function expressed in eq. (3), we obtain the posterior best estimate of $\mathbf{s}$ as [*Enting*, 2002]:

$$\hat{\mathbf{s}} = (\mathbf{M}^{\mathrm{T}}\mathbf{R}^{-1}\mathbf{M} + \mathbf{Q}^{-1})^{-1}(\mathbf{M}^{\mathrm{T}}\mathbf{R}^{-1}\mathbf{c} + \mathbf{Q}^{-1}\mathbf{s_p}). \quad (4)$$

Meanwhile the posterior uncertainty matrix for the posterior flux can be deduced as follows:

$$\hat{\mathbf{Q}} = (\mathbf{Q}^{-1} + \mathbf{M}^{\mathrm{T}}\mathbf{R}^{-1}\mathbf{M})^{-1}. \quad (5)$$

Following the methodology of Deng and Chen (2011), the CO_2 concentration matrix **c** in the above equations is the residual concentration after subtracting the observed concentration with contributions from fossil fuel emission, biomass burning, the prior ocean flux and the prior biospheric flux (see Section 2.4 for detail). In this way, the values in $\mathbf{s_p}$ are set to zero and the inverted flux **s** is considered to be an adjustment to the prior flux that contributes to the pre-subtracted portions of the CO_2 concentration.

2.1.3 Synthesis Bayesian inversion with both CO_2 and $^{13}CO_2$ observations

We attempt to use $^{13}CO_2$ observations to provide an additional constraint to the otherwise CO_2-only inversion presented above. This additional constraint is possible on the grounds that air $^{13}CO_2$ concentration is affected differently by carbon fluxes from ocean and land surfaces. Since the $^{13}CO_2$ gas is transported passively in similar ways as CO_2, the same transport matrix **M** applies to $^{13}CO_2$ data to associate $^{13}CO_2$ observations with the surface$^{13}CO_2$ flux. This simple treatment of the transport matrix differs from Rayner et al. (2008) who considered the additional small impact of mixing of airmasses with different $^{13}CO_2$ concentrations on its long-term transport. In order to conduct an inversion using both CO_2 and $^{13}CO_2$ observations, we simply append $^{13}CO_2$-related data to the **c**, **R** and **M** matrixes in Eq. (4), while the **s** matrix remains unchanged as the purpose of this joint inversion is only to optimize the CO_2 flux. For **c** and **R**, $^{13}CO_2$ observations and their variances are appended directly to the original matrixes for the CO_2 only case, as shown in Eq. 6. Similarly, the **M** matrix is also extended to consider $^{13}CO_2$ transport, and the relevant elements for the $^{13}CO_2$ observation stations are from the original **M** matrix. However these elements are multiplied by the $^{13}CO_2$ discrimination rate over land or ocean for each region and

Geosci. Model Dev. Discuss., doi:10.5194/gmd-2016-53, 2016
Manuscript under review for journal Geosci. Model Dev.
Published: 17 May 2016

Geoscientific Model Development Discussions

each month in order to relate the CO_2 flux to the temporal variations in the measured air $^{13}CO_2$ composition at each station and each month. The extended **M** is a combination of the corrected **M** matrix appended to the **M** matrix for CO_2 (see below)

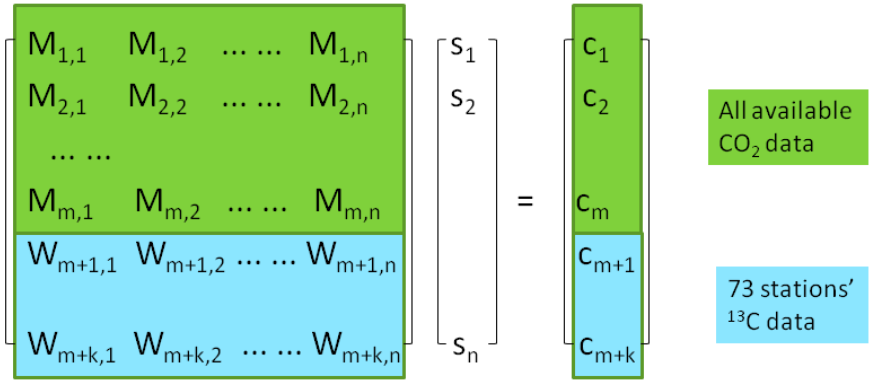

(6)

where c_i is the CO_2 concentration (i=1 to m) and ^{13}C composition (i=m+1 to m+k) in the air from the starting month (i=0); M_{ij} is the transport operator between region-month j (hereafter simply referred as region) and station-month i (hereafter simply referred as station), and $W_{ij} = D_j M_{ij}$, in which D_j is the discrimination rate against $^{13}CO_2$ in the CO_2 flux for region j. In the inversion procedure, the difference in concentration between two consecutive times is equated with the flux during the time interval (one month).

In order to calculate D_j and C_i (i=m+1 to m+k) in Eq. 6, some theoretical development is made according to the $^{13}CO_2$ budget equation derived by Tans et al. (1993):

$$C_a \frac{d\delta_a}{dt} = F_f(\delta_f - \delta_a) - (F_{lph} - F_{lb})\varepsilon_{lph} + F_{lb}(\delta_{lb} - \delta_{lb}^e) - (F_{oa} - F_{oa})\varepsilon_{ao} + F_{oa}(\delta_a^e - \delta_a) \quad (7)$$

where C_a is the CO_2 pool in the atmosphere (in Pg C), δ_a is the ^{13}C composition of the atmosphere in ‰, F_f is the carbon emission from fossil fuels and biomass burning, δ_f is the ^{13}C composition of fossil fuels or biomass, F_{lph} is the photosynthetic carbon uptake by the land biosphere (always positive), F_{lb} is the respiratory carbon flux of the land biosphere (always positive), ε_{lph} is the photosynthetic discrimination of the land biosphere in ‰, δ_{lb} is the ^{13}C composition of the land respiratory carbon flux (see Section 2.2.2), δ_{lb}^e is the biospheric ^{13}C composition in equilibrium with the current atmosphere (i.e. in 2003), F_{oa} is the one-way carbon from the ocean surface to the atmosphere (always positive), F_{ao} is the one-way carbon flux from the atmosphere to the ocean surface (always positive), ε_{ao} is the air-to-ocean fractionation, ε_{oa} is the air-to-ocean fractionation, and δ_a^e is the ^{13}C composition in equilibrium with the ocean surface. Eq. 7 states that the temporal variation of the measured ^{13}C composition in the atmospheric CO_2 is determined by contributions from the various sources: fossil fuels and biomass burning (term 1 of the right hand side of Eq. 7), net land biosphere carbon uptake (term 2), one-way respiratory flux from the land biosphere (term 3), net carbon flux of the ocean (term 4), and one-way ocean-to-atmosphere

Geosci. Model Dev. Discuss., doi:10.5194/gmd-2016-53, 2016
Manuscript under review for journal Geosci. Model Dev.
Published: 17 May 2016

Geoscientific Model Development Discussions

flux (term 5). The one-way carbon fluxes from land and ocean surfaces are important sources of ^{13}C because the atmosphere is in isotopic disequilibrium with these surfaces due to the long-term change of the atmospheric ^{13}C composition. Similar to other terms in Eq. 7, these disequilibrium fluxes are also called isofluxes (*Rayner*, 2001).

In order to reduce the errors of our inversion system (Eq. 6) that assumes linear relationships between fluxes and concentrations, the contributions of all fluxes, including prior biospheric and ocean fluxes, to the CO_2 concentration are subtracted from the measured CO_2 concentration prior to the inversion (*Deng and Chen*, 2011). Accordingly, the contributions of all ^{13}C sources to the ^{13}C concentration in the atmosphere are also subtracted from the measured ^{13}C concentration. The purpose of the inversion is then to find the residual CO_2 flux, denoted as **S** in Eq. 6. For this purpose, we denote S_{lN} =-(F_{lph}-F_{lb}) as the net flux from the land surface to the atmosphere (negative for sinks) and S_{oN} =-(F_{ao}-F_{oa}) as the net flux from the ocean surface to the atmosphere (negative for sinks). After taking $S_{lN} = S_{lN}^P + S_l$ and $S_{oN} = S_{oN}^P + S_o$, where S_{lN}^P and S_{oN}^P are the prior net CO_2 fluxes to the land and ocean surfaces, respectively, and S_l and S_o are the residual fluxes to be inverted for the land and ocean surfaces, respectively, Eq. 7 can be rewritten as:

$$S_l\varepsilon_{lph} + S_o\varepsilon_{ao} = C_a\frac{d\delta_a}{dt} - [F_f(\delta_f - \delta_a) + S_{lN}^P\varepsilon_{lph} + F_{lb}(\delta_{lb} - \delta_{lb}^e) + S_{oN}^P\varepsilon_{ao} + F_{oa}(\delta_a^e - \delta_a)] \qquad \textbf{(8)}$$

Eq. 8 is the theoretical basis for our joint $^{13}C/^{12}C$ inversion as it links the measured ^{13}C composition in the atmosphere to the CO_2 fluxes of the land and ocean surfaces. In the implementation of the joint inversion system (Eq. 6), a transport matrix is used to link a flux in a particular region to the concentration measured at a particular site. We focus on optimizing the net CO_2 flux using both CO_2 and $^{13}CO_2$ observations rather than optimizing the one-way fluxes, and therefore the discrimination terms to be optimized are moved to the left-hand side of Eq. 8 and the disequilibrium terms remain on the right-hand side. Based Eq. 8, the regional discrimination D_j in Eq. 6 is therefore defined as:

$$\begin{aligned} D_j &= \varepsilon_{lph,j} \quad \text{for land} \\ D_j &= \varepsilon_{ao,j} \quad \text{for ocean} \end{aligned} \qquad (9)$$

where $\varepsilon_{lph,j}$ and $\varepsilon_{ao,j}$ are the ^{13}C fractionation ratio for region *j* for land and ocean fluxes, respectively.

For land regions, BEPS is used to calculate all land variables in Eq. 8, including S_{lN}^P, F_{lb}, ε_{lph}, R_{lb}, δ_{lb} and δ_{lb}^e for each region and month. For ocean regions, ε_{ao}=-2‰, and empirical equations developed by *Ciais et al*. (1995b) are used to calculate F_{oa} and δ_a^e as functions of sea surface temperature on 1°×1° grids.

The $^{13}CO_2$ concentration time series (c_{m+1}, … c_{m+k}) in Eq. 6 in ppm‰ is the numerical realization of the right hand side of Eq. 8 and is computed with the following equation:

$$c_i = \overline{C}_{a,i}\frac{d\delta_{a,i}}{dt} - \sum_{k=1}^{5} {}^{13}\delta_k\frac{dC_{k,i}}{dt} \qquad (10)$$

Geosci. Model Dev. Discuss., doi:10.5194/gmd-2016-53, 2016
Manuscript under review for journal Geosci. Model Dev.
Published: 17 May 2016

Geoscientific Model Development Discussions

In Eq.10, $\overline{C}_{a,i}\frac{d\delta_{a,i}}{dt}$ can be calculated with observed CO_2 concentration and ^{13}C composition at two consecutive times, *t* and *t+1*, using the following equation:

$$\overline{C}_{a,i}\frac{d\delta_{a,i}}{dt}=\frac{C_{a,i}^{t+1}+C_{a,i}^{t}}{2}(\delta_{a,i}^{t+1}-\delta_{a,i}^{t}) \quad (11)$$

where $\overline{C}_{a,i}$ is the mean concentration of CO_2 at each observation station *i* between *t* and *t+1*, and $\delta_{a,i}$ is the ^{13}C composition at station *i*, and its derivative with time is taken as its difference between *t* and *t+1*. This derivative represents the δ_a growth rate that is the combined outcome of the various isofluxes in Eq. 7. The term $\sum_{k=1}^{5}{}^{13}\delta_k\frac{dC_{k,i}}{dt}$ is the sum of $^{13}\delta$ changes due to fossil fuel and biomass burning, prior land ^{13}C discrimination flux, land ^{13}C disequilibrium flux, prior ocean ^{13}C discrimination flux, ocean ^{13}C disequilibrium flux, corresponding to the terms in Eq.8. $^{13}\delta_k$ represents $^{13}\delta$ value (‰) for each term in Eq.8, and $\frac{dC_{k,i}}{dt}$ is the change of concentration (ppm) calculated with the flux of each term in Eq.8 according to the atmospheric transport function **M** in Eq.6.

The inversion system defined by Eq. 6 can be implemented in three ways using (1) CO_2 concentration only by excluding the appended matrices for $^{13}CO_2$, (2) $^{13}CO_2$ data only by using $^{13}CO_2$-related matrices only, and (3) both CO_2 and $^{13}CO_2$ data. Through using the data in these three ways, the information content of $^{13}CO_2$ measurements for CO_2 can be systematically investigated.

In order to investigate the influences of the isotopic discrimination and disequilibrium over land and ocean on the inversion results, we conduct five sets of inversions for the following cases: Case I: The spatial variations of all isotopic compositions and the discrimination and disequilibrium fluxes in Eq. 8 are considered for both land and ocean. This is the ideal case as the basis to investigate other cases; Case II: The photosynthetic discrimination (ε_{lph}) over land is taken as a constant of -14.1‰, which is the global average obtained by BEPS, and therefore D_j=-14.1‰. This is a case to ignore regional differences in isotopic discrimination over land; Case III: All isotopic variables are the same as Case I, but the land disequilibrium term in Eq. 8 is ignored. This is a case to investigate the influence of the land isotopic disequilibrium on the CO_2 flux inversion; Case IV: All isotopic variables are the same as Case I, but the ocean disequilibrium term in Eq. 8 is ignored. This is a case to investigate the influence of the ocean isotopic disequilibrium on the CO_2 flux inversion; and Case V: Both land and ocean disequilibrium terms are ignored, but all other isotopic variables in Eq. 8 are same as Case I. This is a case to investigate the importance of the total disequilibrium flux in CO_2 flux inversion at the global scale. Cases III to V are useful not only for evaluating the performance of the joint inversion system but also for assessing the impacts of errors in isotopic disequilibrium estimation on the CO_2 flux inversion.

2.1.4 Covariance matrixes for the CO_2 flux and CO_2 and $^{13}CO_2$ concentration measurements

Geosci. Model Dev. Discuss., doi:10.5194/gmd-2016-53, 2016
Manuscript under review for journal Geosci. Model Dev.
Published: 17 May 2016

In the joint inversion using both CO_2 and $^{13}CO_2$ measurements, the covariance matrix (**Q**) for the CO_2 flux remains the same as that in the CO_2 only inversion (Eq. 3) but the error matrix (**R**) for concentration measurements is expanded to the dimension of 16980×16980 to include 60 months of $^{13}CO_2$ observations at 73 stations. Following *Deng and Chen* (2011), we use an uncertainty of 2.0 Pg C y^{-1} for the total global land surface CO_2 flux, and this total uncertainty is spatially distributed to the 39 regions according to the annual total NPP of these regions simulated by BEPS. For each region, the annual total uncertainty is further distributed to each month according to the simulated seasonal variation in NPP. The global total uncertainty (standard deviation) is spatially and temporally distributed in such a way that the total variance is preserved after the distributions, following the principle of TRANSCOM 3 (Gurnay et al., 2003). The uncertainty for the total ocean flux is prescribed as 0.67 Pg C y^{-1} (*Deng and Chen*, 2011). In this way, all the diagonal elements (Q_{ii}) in the uncertainty matrix **Q** are determined, while off-diagonal values are assigned to zero, meaning that no flux covariances between regions and months are assumed. The uncertainty of CO_2 measurements in the **R** matrix is the same as that described in *Deng and Chen* (2011), following the approach of *Peters et al*. (2005) and *Bakers et al*. (2006). In this approach, the uncertainty of a monthly CO_2 measurement at a site is estimated as $R_{ii} = \sigma_{const}{}^2 + GVsd^2$, where constant portion σ_{const} in ppm is assigned according to site category: Antarctic (0.15) , oceanic (0.30), land and tower (1.25), mountain (0.90), and aircraft (0.75), while the site-specific variable portion $GVsd$ is obtained from the GLOBALVIEW-CO2 2008 database. The $^{13}CO_2$ measurement uncertainty is calculated in a similar way: the variable portion is obtained from the GLOBALVIEW-13CO2 2008 database, while the constant portion is taken as $R_a\sigma_{const}$ in ppm first, where R_a is the ratio of $^{13}CO_2$ to CO_2 in the air (~0.011147), and then converted to ‰. The average standard deviation of $\delta^{13}C$ observations determined in this way for 73 stations is 0.0685‰.

2.2 Prior CO_2 and $^{13}CO_2$ flux estimation

2.2.1 CO_2 flux

Terrestrial biosphere fluxes

A process-based terrestrial ecosystem model called the Boreal Ecosystem Productivity Simulator (BEPS) (*Chen et al.*, 1999; *Liu et al.*, 1997) is used in this study to estimate the net terrestrial CO_2 flux and its components including the gross primary productivity (GPP), net primary productivity (NPP), heterotrophic respiration (F_{lb}), and net ecosystem productivity (NEP). GPP is calculated using the Farquhar's leaf-level model (*Farquhar et al*, 1980) upscaled to the canopy level using a recently refined two-leaf approach (*Chen et al*., 2012). NPP is taken as 45% of GPP (*Ise et al*., 2010) as global biomass data and its components (stem, foliage, root) are lacking for reliable computation of the autotrophic respiration. F_{lb} is calculated as the sum of the decompositional CO_2 release from 9 soil carbon pools, namely coarse and dead wood detritus pool, surface structural pool, surface metabolic pool, surface microbial pool, fine-root structural litter pool, fine-root metabolic pool, soil

Geosci. Model Dev. Discuss., doi:10.5194/gmd-2016-53, 2016
Manuscript under review for journal Geosci. Model Dev.
Published: 17 May 2016

microbial pool, slow carbon pool, and passive carbon pool. The sizes of these pools for each cover type in each 1º grid are estimated using a model spin-up approach based on simulated NPP in 2000 to create a global land sink of 3.73 Pg C y^{-1}. The total NPP for each 1º grid is taken as a weighted sum of NPP of 7 aggregated land cover types, and the weights are proportional to the areal fractions of the cover types determined using the GLC2000 land cover map at 1 km resolution (*Chen et al*., 2012). Remotely sensed LAI [*Deng et al.*, 2006] at 1 km resolution and a clumping index map at 6 km resolution (*Chen et al*., 2005) and a soil textural map (*Webb et al*., 1991) are aggregated to 1º grids for each cover type based on GLC2000 land cover and used as input to BEPS. National Center of Environmental Prediction (NCEP) reanalyzed data [*Kalnay et al*., 1996; *Kanamittsu et al*.,2002] are the meteorological drivers for BEPS to simulate hourly carbon fluxes.

Ocean fluxes

The daily flux of CO_2 across the air-water interface used in this study is constructed based on the results of daily CO_2 fluxes simulated by the OPA-PISCES-T model [*Buitenhuis et al.*, 2006]. This model is a global ocean general circulation model (OPA) [*Madec et al*., 1998] coupled to an ocean biogeochemistry model (PISCES-T) [*Aumont et al.*, 2003; *Buitenhuis et al.*, 2006]. PISCES-T represents the full cycles of C, O_2, P, Si, total alkalinity and a simplified Fe cycle. It also includes a representation of two phytoplankton, two zooplankton and three types of dead organic particles of different sinking rates. OPA-PISCES-T is forced by daily wind stress and heat and water fluxes from the NCEP reanalyzed data [*Kalnay et al.*, 1996*, Kanamittsu et al.,2002]*. Hourly S_o (^{13}C) is calculated with gridded optimum interpolation sea surface temperature of NOAA National Climate Data Center (*Reynolds and Smith*, 1994; *Reynolds et al*., 2002).

Fossil-fuel emissions

The fossil fuel emission field (2000-2004) used in this study (http://carbontraacker.noaa.gov) is constructed based on (1) the global, regional and national fossil-fuel CO_2 emission inventory from 1871 to 2006 (CDIAC) [*Marland et al.*, 2009], and (2) the EDGAR 4 database for the global annual CO_2 emission on a 1˚ grid [*Olivier et al.*, 2005]. The $^{13}CO_2$ flux from fossil-fuel consumption is calculated from CO_2 emissions of different fuel types multiplied by their respective $^{13}C/^{12}C$ ratios with consideration of their latitudinal distributions based on *Andres et al.* (2000).

Fire emissions

CO_2 emissions due to vegetation fires are an important part of the carbon cycle [*van der Werf et al.*, 2006]. Each year, vegetation fires emitted around or more than 2 PgC of CO_2 into the atmosphere, mostly in the tropics. The fire emission field used in this study is based on the Global Emissions Fire Database version 2 (GFEDv2) (*Randerson et al.*, 2007; *van der Werf et al.*, 2006)

2.2.2 $^{13}CO_2$ flux

Based on the initial work of *Chen et al*. (2006), BEPS is further developed to include a capacity to compute the global distribution of the terrestrial $^{13}CO_2$ flux. Following the principle of multi-stage ^{13}C fractionation in the pathway through leaf boundary layer, stomates, messophyll and chloroplast initially proposed by *Farquhar et al*. (1984, 1989) and

Geosci. Model Dev. Discuss., doi:10.5194/gmd-2016-53, 2016
Manuscript under review for journal Geosci. Model Dev.
Published: 17 May 2016

implemented globally by *Suits et al*. (2005), we developed a module in BEPS for computing the total photosynthetic fractionation and the resultant $^{13}CO_2$ flux. Specifically, the photosynthetic discrimination for C3 plants (Δ_{PC3}) is calculated from

$$\Delta_{PC3} = \frac{pA}{C_a}\left[\frac{\Delta_b}{g_b} + \frac{\Delta_s}{g_s} + \frac{\Delta_{diss} + \Delta_{aq}}{g_m}\right] + \frac{C_c}{C_a}\Delta_f \quad (12)$$

where Δ_b, Δ_s, Δ_{diss}, Δ_{aq}, and Δ_f are the rates of discrimination against $^{13}CO_2$ through leaf boundary layer, stomates, dissolution in mesophyll water, transport in aqueous phase, and fixation in chloroplast, respectively, and are assigned values of 2.9‰, 4.4‰, 1.1‰, 0.7‰ and 28.2‰, respectively (*Suits et al*., 2005). A is the photosynthetic rate in mol m^{-2} s^{-1} and p equals to $0.022624T_a/(273.16P)$ with the dimension of m^3mol^{-1}, where T_a is air temperature in ºK and P is the standard air pressure at 1.013Bar. C_a and C_c are the CO_2 concentrations in mol mol^{-1} in the free air and leaf chloroplast, respectively. For C4 plants, the photosynthetic discrimination (Δ_{PC4}) is taken as a constant of 4.4‰ (*Suits et al*., 2005).

The leaf boundary-layer (g_b) is calculated with the following equation

$$g_b = \frac{\alpha N}{0.5l} \quad (13)$$

where α is the diffusivity of CO_2 in dry air in m^2s^{-1} calculated as $10^{-6}(0.129+0.007T_a)$ and T_a is the air temperature in ºC; l is the leaf characteristic dimension in m, taken as a constant of 0.1 m; and N is the Nusselt number equal to $(u_d l/\upsilon)^{0.5}$, where u_d is the wind speed in m s^{-1}at the vegetation displacement height (80% of the average vegetation height) and υ is the kinematic viscosity of dry air in m^2 s^{-1} calculated as $10^{-6}(0.133+0.007T_a)$. u_d is derived from the wind speed above the canopy based on LAI and vegetation height assigned according to plant functional type (Table 1).

As part of the GPP calculation, the stomatal conductance (g_s) computed separately for sunlit and shaded leaves using the Ball-Berry equation (Ball, 1988),

$$g_s = f_w(m\frac{A\,h_s}{C_s}p + b) \quad (14)$$

where f_w is a scaling factor depending on soil moisture and texture (*Chen et al.*, 2012); h_s is the air humidity at the leaf surface; C_s is the CO_2 concentration at the leaf surface; p is the same as in Eq. 12; and m and b are the slope and intercept in this linear relationship, and they are assigned values according to plant function type (Table 1) (*Chen et al*., 2012).

The mesophyll conductance g_m is calculated based on the method of Harley (1992):

$$g_m = \frac{A}{C_i - \frac{\Gamma\cdot[J+8\cdot(A+R_d)]}{J-4\cdot(A+R_d)}} \quad (15)$$

where A is the photosynthetic CO_2 assimilation rate; C_i is partial pressure of CO_2 in the air spaces inside leaves; R_d is the respiration rate occurring during the day not related to photorespiration; Γ is the CO_2 compensation point in the absence of

Geosci. Model Dev. Discuss., doi:10.5194/gmd-2016-53, 2016
Manuscript under review for journal Geosci. Model Dev.
Published: 17 May 2016

Geoscientific Model Development Discussions

R_d; and J is the rate of photosynthetic electron transport. These parameters are the same as those used in computing the CO_2 flux.

Our methods of computing stomatal and mesophyll conductances differ from previous studies (*Suits et al*., 2005; *Scholz et al*., 2008; *Rayner et al*., 2008) in the following ways: (1) these conductances are calculated separately for sunlit and shaded leaves because BEPS is a two-leaf model, in which the total GPP of a canopy is taken as the sum of sunlit and shaded leaf GPP; and (2) the mesophyll conductance mechanistically depends on a set of parameters rather than being treated as a constant or to be proportional to the stomatal conductance. Since it has been demonstrated that sunlit and shaded leaf separation is essential for accurate modeling of canopy-level photosynthesis (*Chen et al*., 1999; *Sprintsin et al*., 2011), it is expected that this separation is also essential for $^{13}CO_2$ flux estimation. We found that the use of Harley's method for computing the mesophyll conductance makes the calculated ^{13}C photosynthetic fractionation stable for its global application, while the simpler method of treating the mesophyll conductance in proportion with the stomatal conductance often incurs abnormally large or small values of ^{13}C photosynthetic fractionation.

The photosynthetic $^{13}CO_2$ flux is in disequilibrium with the respiratory $^{13}CO_2$ flux because of the change in atmospheric $^{13}CO_2$ concentration since the preindustrial time (*Ciais et al*., 1995b; *Fung et al*., 1997). The heterotrophic respiratory flux from the decomposition of organic matter of different ages carries the memory of the past atmospheric $^{13}CO_2$ concentration, while the photosynthetic $^{13}CO_2$ flux is affected by the current atmospheric $^{13}CO_2$ concentration. The isotopic composition of each of the 9 soil carbon pools ($\delta^{13}C_{soil,\,i}$) is estimated with following formula:

$$\delta^{13}C_{soil,\,i} = \delta^{13}C_a\,(2003\text{-}\tau_i) - \varepsilon_{lph} \qquad (16)$$

where $\delta^{13}C_a$ is the isotopic composition of carbon in atmosphere CO_2 in the past as determined by the ice-cord record (*Francey et al*., 1999); ε_{lph} is the annual mean of photosynthetic discrimination in 2003; and τ_i is the age of carbon pool i (Table 2) (*Ju et al*., 2005). In the calculation of the mean age of a carbon pool, we have considered the ages of various carbon pools at the time of entering the pool (*Potter et al., 1993*), so that the mean age is considerably larger than the turnover time determined by the decomposition rate (*Fung et al., 1997*). The mean $\delta^{13}C_{soil}$ is taken as the flux-weighted $\delta^{13}C_{soil,i}$ for the 9 carbon pools. The results of $\delta^{13}C_{soil}$ for the globe are shown in Figure 5. The ^{13}C composition of the biosphere δ_{lb} in Eq. 8 is taken as the mean $\delta^{13}C_{soil}$, while the biospheric ^{13}C composition δ^{e}_{lb} in equilibrium with the current atmosphere is taken as δ_a - ε_{lph}.

The accuracy of the BEPS model in simulating atmospheric $^{13}CO_2$ concentration was previously tested (*Chen et al*., 2006; *Chen and Chen*, 2007) against measurements over a boreal forest at Fraserdale, Ontario, Canada (49◦52'29.9''N, 81◦34'12.3''W). Flask measurements of $\delta^{13}C_a$ were made 40 times in both daytime and nighttime on a tower at a height of 20 m during a 3-day campaign on 21-23 July 1999. BEPS simulated these measurements with RMSE=0.34‰ and r^2=0.76.

2.3 Transport modeling

Geosci. Model Dev. Discuss., doi:10.5194/gmd-2016-53, 2016
Manuscript under review for journal Geosci. Model Dev.
Published: 17 May 2016

A transport-only version of the atmospheric chemistry and transport model TM5 (*Krol et al.*, 2003; *Krol et al.*, 2005) is used for CO_2 and $^{13}CO_2$ transport modeling to produce a fully linear operator on these fluxes. Tracer transport (advection, vertical diffusion, cloud convection) in TM5 is driven by offline meteorological fields taken from the European Centre for Medium Range Weather Forecast (ECMWF) model. All physical parameterizations in TM5 are kept the same as the ECMWF formulation to achieve compatibility between them. The four background fluxes from terrestrial ecosystems, oceans, fossil-fuel burning, and biomass burning are individually inputted to TM5 to calculate the contributions of these fluxes to the atmospheric CO_2 and $^{13}CO_2$ concentrations.

2.4 CO_2 and $^{13}CO_2$ datasets

Monthly CO_2 and $^{13}CO_2$ concentration data from 2000 to 2004 are compiled from the GLOBALVIEW CO_2 and $^{13}CO_2$ database. Though the GLOBALVIEW database consists of both extrapolated and interpolated data that were created based on the technique devised by *Masarie and Tans* [1995], we selected the synchronized and smoothed values of actual observations to compile our concentrations datasets. Only direct measurements of CO_2 from the GlobalView dataset are used in our inversion after using a time-frequency weighting scheme (Deng and Chen, 2011). There are 5431 monthly data from 209 sites for 42 months used for CO_2 (5431 out of 8778, i.e. 209×42), and 3066 monthly data from 73 sites for $^{13}CO_2$ (i.e. 73×42 monthly data). Since the number of $^{13}CO_2$ observation sites is much smaller than that of CO_2 sites, all monthly data at 73 sites are used for $^{13}CO_2$, and the missing $^{13}CO_2$ data are filled with the reference data provided in the same GlobalView dataset. The filled data may have introduced an additional error to the dataset as shown in Figure 15b.

To minimize the nonlinear aggregation effects of the large regions (*Pickett-Heaps*, 2007), the contributions of the four background fluxes are subtracted from the above monthly concentrations. So the matrix $\mathbf{c}$ in Eqs. (3) and (4) is expressed as

$$\mathbf{c} = \mathbf{c}_{obs} - \mathbf{c}_{ff} - \mathbf{c}_{bio} - \mathbf{c}_{ocn} - \mathbf{c}_{fire} \quad (17)$$

where $\mathbf{c}_{obs}$ is the monthly CO_2 and $^{13}CO_2$ concentrations obtained from GLOBALVIEW, and $\mathbf{c}_{ff}$, $\mathbf{c}_{bio}$, $\mathbf{c}_{ocn}$, and $\mathbf{c}_{fire}$ are simulated contributions of CO_2 and $^{13}CO_2$ concentrations from the terrestrial biosphere, ocean, fossil-fuel, and fire fluxes, respectively.

3. Results

3.1 Prior CO_2 and $^{13}CO_2$ fluxes

Terrestrial ecosystem models integrate many sources of information, including vegetation structure, soil, and meteorology, to estimate carbon exchange of the land surface with the atmosphere. Prior CO_2 and $^{13}CO_2$ fluxes produced by a model can therefore provide indispensible constraints to the otherwise ill-posed inversion based on CO_2 and $^{13}CO_2$

Geosci. Model Dev. Discuss., doi:10.5194/gmd-2016-53, 2016
Manuscript under review for journal Geosci. Model Dev.
Published: 17 May 2016

concentration observations alone. Depending on the assigned relative magnitudes of the error matrixes of these observations and these prior fluxes (i.e., **R** and **Q** in Eq. 3), these prior fluxes can have equal or even dominant importance to these observations in the inversion results. We have therefore paid a great attention in modeling these prior fluxes, in order to minimize the total inversion errors. Figure 2a shows an example of the global terrestrial GPP distribution in 2003 modeled by BEPS. The total GPP in this year is 132±22 Pg C y^{-1} (*Chen et al*., 2012). This value is larger than some of the recent estimates, such as 123 Pg C y^{-1} by *Beer et al*. (2010), mostly because the LAI values used as input to BEPS are generally larger than those of the MODIS product (*Garrigues et al*., 2008). Our LAI values are larger because we used a global clumping index map derived from a multi-angle satellite sensor POLDER (*Chen et al*., 2005). Clumping increases shaded leaves which contributed about 35% to the total GPP globally. Without considering this clumping effect, the shaded leaf area is underestimated, resulting in an underestimation of the global GPP by 9% (*Chen et al*., 2012). As the spatial distribution of clumping is not uniform (boreal and tropical forests are most clumped and crops and grasses are least clumped), this refinement in the GPP spatial distribution would have some effects on the inversion results between regions.

The net ecosystem productivity (NEP), which is the difference between GPP and ecosystem respiration modeled by BEPS, is shown in Figure 2b for 2003. Even though GPP has a large uncertainty (globally 22 Pg C y^{-1} by BEPS), the uncertainty in NEP is much smaller (globally 2 Pg C y^{-1} by BEPS) because a model spin-up approach is used to estimate the soil carbon pool sizes based on a dynamic equilibrium assumption. Under this assumption, the annual heterotrophic respiration (F_{lb}) equals annual NPP during the preindustrial period, and the soil carbon pool sizes are derived from F_{lb} by solving a set of differential equations describing the decomposition and interactions among the pools (*Govind et al*., 2011). In this way, F_{lb} is forced to depend on NPP and the systematic biases in GPP are not carried into NEP estimation. NEP is non-zero after the preindustrial period because of the changes in climate and atmospheric composition (CO_2 and nitrogen) as well as disturbance. In our regional modeling, both disturbance and non-disturbance effects are considered for Canada (*Chen et al*., 2003) and USA (*Zhang et al*., 2012) forests. However, in our global model spin-up from 1901 (taken as the end of preindustrial period) to 2000, only the non-disturbance effects are considered because of lack of spatially explicit disturbance data outside of North America, while carbon emission due to fire disturbance in the study period from 2000 to 2004 is considered separately using the GFED dataset (*Randerson et al*., 2007; *van der Werf et al*., 2006). The prior net CO_2 fluxes for the globe for the years 2002-2004 are given in Table 3 with inversion results with and without the ^{13}C constraint.

The global distribution of the total photosynthetic discrimination ($\delta^{13}C_{pt} = \delta^{13}C_a - \Delta$) modeled by BEPS is shown in Figure 3. Forests, such as those in North America, Russia, Europe, Amazon, central Africa, central China and southeast Asia, generally have high photosynthetic discrimination rates (>16‰), while grassland and cropland (in particular C4 grasses and crops) have low discrimination rates. Also shown in Figure 3 is the ocean diffusive discrimination against $^{13}CO_2$. The discrimination over ocean is much smaller than that over land. This difference between land and ocean discrimination may be considered as the largest signal of $^{13}CO_2$ observations on the global carbon cycle (*Tans et al*., 1990;

Geosci. Model Dev. Discuss., doi:10.5194/gmd-2016-53, 2016
Manuscript under review for journal Geosci. Model Dev.
Published: 17 May 2016

Rayner et al., 2008) and is considered in our inversion using different $^{13}CO_2$ discrimination rates for ocean and land regions (see Eq. 6).

To estimate the disequilibrium between photosynthetic and respiratory discrimination against $^{13}CO_2$, the global distribution of the mean soil carbon age is computed after weighting the ages of the 9 soil carbon pools against their fluxes due to decomposition (Figure 4). Forests at high latitudes have the soil carbon age of about 40-60 years, while the tropical forests have much lower values in the range from 10 to 30 years. This latitudinal distribution pattern is mostly determined by soil temperature. In low latitudes, high temperature induces fast turnovers of detritus and fast soil carbon pools, while at high latitudes, low temperature maintains relatively large fractions of slow and passive soil carbon pools. Cropland and grassland also have larger fractions of fast and detritus carbon pools than forest cover types and therefore have younger soil carbon on average. This spatial distribution of soil carbon age has a strong influence on the total respiratory discrimination against ^{13}C ($\delta^{13}C_r$) calculated by BEPS (Figure 5). Respiration from older carbon at high latitudes carries the memory of the older atmosphere with less $^{13}CO_2$ concentration and hence has lower discrimination rates (larger $\delta^{13}C_r$ or smaller absolute value). However, respiration would mostly depend on the photosynthetic discrimination rates as soil organic matter originates from photosynthetic production. As a result, forested areas have higher respiratory discrimination rates (lower $\delta^{13}C_r$ or larger absolute value). Most of the high values of $\delta^{13}C_r$ in Figure 5 are associated with large fractions of C4 plants in the grid, such as the corn belt in the USA, cropland in northeast China, southern border of Sahara desert, and southeast South America. The global distribution of the disequilibrium between photosynthetic and respiratory discrimination, taken as the difference between Figure 3 and Figure 5, is shown in Figure 6. The disequilibrium is the largest at high latitude boreal forests in North America and Eurasia because their soil carbon is the oldest, as shown in Figure 4. The spatial distribution pattern of the disequilibrium is similar to those of *Ciais et al*. (1995b) and *Fung et al*. (1997) but the magnitude is larger because the date of our result in 2000 is more recent than these two previous studies. As the time lapses, the atmosphere is getting lighter in terms of the isotopic composition of CO_2 resulting from the increased air-borne CO_2 from fossil fuel consumption. Also shown in Figure 6 is the disequilibrium over the ocean estimated using the method of *Ciais et al*. (1995b). This ocean disequilibrium has a large latitudinal gradient because of the gradients in sea surface temperature gradient and the fluxes of CO_2 and $^{13}CO_2$. The spatial distribution in the disequilibrium and the differences in disequilibrium between ocean and land may be considered to be the secondary signal of $^{13}CO_2$ observations on the global carbon cycle. The effects of these disequilibria on the carbon flux are considered in our inversion through presubtracting their contributions to the measured $^{13}CO_2$ composition in Eq. 10.

3.2 Inverse modeling results

Although the inversions were made for the 2000-2004 period, the results of the first two years are not included in the analysis because they are affected by the assumption of uniform global distributions of CO_2 and $^{13}CO_2$ concentrations at the

Geosci. Model Dev. Discuss., doi:10.5194/gmd-2016-53, 2016
Manuscript under review for journal Geosci. Model Dev.
Published: 17 May 2016

start of our transport modeling using TM5. An 18-24 month period is usually considered to be necessary for the simulated distributions to reach realistic states with reasonably accurate prior surface fluxes from ocean and land and atmospheric transport simulations (*Rödenbeck et al*., 2003; *Deng and Chen*, 2011). The following results are therefore summarized as the average for the 2002-2004 period.

3.2.1 Partition between ocean and land sinks with and without $^{13}CO_2$ constraint

To investigate the usefulness of $^{13}CO_2$ observations in partitioning between ocean and land sinks, we conducted inversions with and without $^{13}CO_2$ constraint as expressed in Eq. 6, i.e. with and without the ^{13}C-related expansions of the matrixes. The CO_2-only inversion increases the land sink from the prior of 2.61 PgC y^{-1} to 3.40 PgC y^{-1} while decreasing the ocean sink from the prior of 2.13 PgC y^{-1} to 1.48 PgC y^{-1} (Table 3). These results are similar to those of *Deng and Chen* (2011). The results from the joint inversion are considerably different: the posterior sinks for land and ocean become 2.78 and 2.25 PgC y^{-1} (Table 3), respectively, suggesting that the use of $^{13}CO_2$ observations in the inversion considerably influenced the partition between land and ocean fluxes. The ratio between land and ocean sinks is 1.24. The joint inversion system developed in this study may be regarded as a different form of double deconvolution. Using the double deconvolution method with the global average disequilibrium coefficients of 0.49‰ and 0.78‰ and the disequilibrium fluxes of 26.8 PgC y^{-1} ‰ and 66 PgC y^{-1} ‰ for land and ocean derived in this study (Table 4), respectively, we also calculated the land and ocean sinks to be 2.90 and 2.36 PgC y^{-1}, respectively. The ratio between land and ocean sinks is 1.23, which is very close to the value of 1.24 derived from the joint inversion system, indicating that the joint inversion can effectively perform double deconvolution. Our joint inversion system differs from previous double deconvolution systems (*Siegenthaler and Oeschger*, 1987*; Keeling et al.*, 1989a; *Francey et al*., 1995; *Randerson et al*., 2002) in the following ways: (1) the estimation of CO_2 fluxes for the land and ocean is additionally constrained by the prior fluxes for the land and ocean rather than entirely dependent on measured CO_2 concentration and $^{13}CO_2$ composition; and (2) the spatio-temporal variations in all parameters associated with isotopic discrimination and disequilibrium are considered in the estimation of the CO_2 flux using a mechanistic biospheric model rather than global average values or simple models based on covariates. These differences in methodology as well as the differences in the mean disequilibrium fluxes may explain why the ocean and land sinks from the joint inversion system differ from the various double deconvolution results.

The impacts of $^{13}CO_2$ data on the joint inversion can also be evaluated from the view point of global $^{13}CO_2$ mass budget. Table 5 shows the budgets and its components for the prior, double deconvolution, CO_2-only inversion and joint inversion cases. In these cases, the isofluxes due to fossil fuel emission, land and ocean disequilibrium, and atmospheric storage change are the same, and only those due to discrimination over land and ocean are adjusted. The prior case shows a global imbalance of -5.0 PgC y^{-1} ‰, indicating that either the prior land or ocean fluxes or both are inconsistent with $^{13}CO_2$ measurements. Through double deconvolution, this imbalance is greatly reduced to 0.8 PgC y^{-1} ‰, mostly by an increase in the discrimination flux over land because of its large discrimination rate. The CO_2-only inversion increases the land discrimination flux while decreasing the ocean discrimination flux, resulting in no improvement in the global isotopic balance. The joint inversion optimized both ocean and land fluxes in the direction consistent with $^{13}CO_2$ measurements,

Geosci. Model Dev. Discuss., doi:10.5194/gmd-2016-53, 2016
Manuscript under review for journal Geosci. Model Dev.
Published: 17 May 2016

Geoscientific Model Development Discussions

reducing the imbalance considerably to 1.8 PgC y^{-1} ‰. These cases illustrate clearly that the global isotopic mass balance is very sensitive to the partition between ocean and land fluxes because of the large difference in the discrimination rate between land and ocean. In this analysis, the disequilibrium fluxes are not adjusted, but the influences of the uncertainties in these fluxes on the inversion results are analyzed in Section 3.2.4.

Existing estimates for the ocean sink for anthropogenic CO_2 in 2000's varies from 1.94 to 2.6 Pg C y^{-1} (*Wanninkhof et al.*, 2013; *Landchuster et al.*, 2014; *Majkut et al.*, 2014; *DeVries*, 2014). The average ocean sink for the 2002-2004 period summarized by the Global Carbon Project (GCP) (*Le Quéré et al.*, 2013) is 2.4 Pg C y^{-1}, while the land sink in the same period is 2.7 Pg C y^{-1} as the residual of the global carbon budget after including the emission due to land use change as a source of carbon. Although the prior estimates of these sinks in our inversions are similar to these values, our CO_2-only inversion considerably increases the land sink and decreases the ocean sink. The addition of $^{13}CO_2$ measurements to the inversion significantly decreases the land sink and increases the ocean sink, pulling the inversion results in the direction to agree with these existing estimates (Figure 7). This may indicate that the use of $^{13}CO_2$ measurements in the joint inversion has improved the CO_2 estimation. In this comparison, we have not considered the unknown small amount (0.1-0.3 Pg C y^{-1}) of lateral carbon transport in rivers from land to ocean. This amount is included in some of the estimates of the ocean sink used by GCP, and therefore should be subtracted from the ocean sink and added to the land sink by GCP in order to compare with our atmospheric inversion results.

3.2.2 Influence of $^{13}CO_2$ constraint on the spatial distribution of the inverted carbon flux

The $^{13}CO_2$ constraint not only modified the partition between ocean and land fluxes but also their spatial distribution patterns. Figure 8 shows the result of the CO_2-only inversion (i.e. without the $^{13}CO_2$ constraint), as the net carbon flux over land and ocean averaged for the period of 2002-2004. Figure 9 shows the difference between inversions with and without the $^{13}CO_2$ constraint, i.e. the result of CO_2+$^{13}CO_2$ inversion minus that of CO_2–only inversion. The general patterns of the inverted carbon flux are similar between these two inversions because these inversions depend primarily on the CO_2 concentration, the prior flux, the error matrixes of the prior flux, and concentration observations. However, there are several large or notable differences: (1) The Amazon region (Region 31) is changed from a carbon source to a sink (Figure 10. Note: a reduction in sources is shown as a negative value); (2) the carbon sink in the tropical Asia (Region 37) is noticeably reduced (by about 10-20 gC $m^{-2}y^{-1}$ from a sink magnitude of about 80-100 gC $m^{-2}y^{-1}$); (3) The sink in Asia (Region 36) decreases pronouncedly by about 10-20 gC $m^{-2}y^{-1}$, while the sinks in Russia (Region 35) and Europe (Region 39) are also reduced by some extents (about 5-20 gC $m^{-2}y^{-1}$); (4) most small regions in the southern part of North America show increases in sinks, but those in the northern part (Canada and Alaska) show increases in sources (see also Figure 11). The overall sink in North America decreases from 0.67 to 0.59 Pg C y^{-1} (Figure 9); and (5) most ocean regions at mid-latitudes have small gains in sink.

It is of particular importance to note that the $^{13}CO_2$ constraint changed the Amazon region from a carbon source of 0.43 ± 0.46 Pg C y^{-1} to a carbon sink of 0.15 ± 0.31 Pg C y^{-1} with a notable reduction in the posterior uncertainty, which is higher than uncertainty reductions in most other regions (Figure 10). This change is likely caused by the relatively large

Geosci. Model Dev. Discuss., doi:10.5194/gmd-2016-53, 2016
Manuscript under review for journal Geosci. Model Dev.
Published: 17 May 2016

addition of information from $^{13}CO_2$ in this tropical region where CO_2 observations are sparse. *Potter et al.* (2009) simulated the net ecosystem productivity (NEP) of the Amazon region using the CASA model driven by remote sensing inputs and found that the NEP for the region was slightly negative (-0.07 Pg C y^{-1}) over the 2000-2004 period. *Davidson et al.* (2012) summarized from various inventory-based studies that mature forests in the region was accumulating carbon at a rate of 0.29-0.57 Pg C y^{-1} over the decade before 2005, meaning that NEP is positive. Since the fire emission is estimated to be 0.50 Pg C y^{-1} (*Richey et al.*, 2002), the Amazon region would be either net source of carbon or about carbon neutral. Since spatially explicit fire emission is considered together with fossil fuel emission as a source in our study, the inverted carbon flux corresponds to –NEP, and therefore the result from our joint inversion is in broad agreement with Potter's and Davidson's results. Without the $^{13}CO_2$ constraint, our inversion result shows an unreasonably large source of carbon in the Amazon region.

3.2.3 Influence of the spatial distribution of photosynthetic discrimination on the inverted carbon flux

The joint inversion results shown in Figures 9 to 11 are from Case I with the best estimates of the ^{13}C discrimination and disequilibrium fluxes and therefore represent a baseline study to which other cases are compared for the purpose of investigating the importance of accurate consideration of the spatial distributions of isotopic discrimination and disequilibrium over land and ocean. Case II is designed to investigate the importance of considering the spatial distribution of the photosynthetic isotopic discrimination over land for inverting the CO_2 flux by fixing the discrimination at a constant over land. Figure 12a shows the spatial distribution of the difference in the total isotopic discrimination, i.e. $D_j = \varepsilon_{lph,j}$, among 39 land regions between Case I and Case II, calculated as Case I minus Case II. Regions with positive differences in D_j are shown with positive differences in the inverted CO_2 flux (Figure 12b), meaning larger sinks (negative values) in Case II, and vice versa. This is because a smaller discrimination rate (smaller than -14.1‰) means a larger CO_2 flux from the atmosphere to the surface (more negative value) for the same change in $^{13}CO_2$ concentration in the atmosphere. Under the same condition, a larger discrimination induces a smaller sink (less negative). The absolute regional differences between Case I and Case II are considerable (Figure 12b), e.g. up to 18 g C $m^{-2}y^{-1}$, showing increases in sinks in Africa, Asia and Australia and decreases in sinks in Amazon, Europe, Russia and most of the small regions in North America. However, the total global sink values of Case II after ignoring the spatial distribution of the disequilibrium rate over land change very little from those of Case I (Table 3): from 2.78±0.76 to 2.72±0.77 Pg C y^{-1} for land and from 2.26±0.35 to 2.23±0.34 Pg C y^{-1} for ocean. This is because the global mean discrimination rates are the same between these two cases.

3.2.4 Influence of the uncertainties in disequilibrium fluxes on the inverted carbon flux

The average disequilibrium coefficients and fluxes for land and ocean derived in this study are comparable to published results (Table 4), although the estimates of the disequilibrium flux over ocean in previous studies vary in a large range. The uncertainty in the estimated land and ocean disequilibrium fluxes mainly arises from two sources: the estimated disequilibrium coefficient and one-way CO_2 flux from the surface. Mathematically, the total uncertainty in the disequilibrium flux, denoted as $\Delta(\delta \cdot F)$, equals the sum of $\Delta\delta \cdot F$ and $\Delta F \cdot \delta$. For land, the first source depends on the modeled

Geosci. Model Dev. Discuss., doi:10.5194/gmd-2016-53, 2016
Manuscript under review for journal Geosci. Model Dev.
Published: 17 May 2016

mean soil carbon age by BEPS, which is estimated to be ±5 years, causing an error in the disequilibrium coefficient to be ±0.11‰ based on the slope of δ_a against time at about 1979 (the flux-weighted global mean soil carbon age is 24 years). The second source is estimated to be 9.5 PgC y^{-1} in NPP, which is taken as 45% of the error in GPP, i.e. 21 PgC y^{-1} (*Chen et al.*, 2012). With NPP=59.4 PgC y^{-1} and the mean disequilibrium efficient of 0.49‰, the uncertainty in the estimated land disequilibrium flux is therefore ±(0.11×59.4 + 0.49×9.5= 11.2 PgC y^{-1} ‰. For ocean, the error in the modeled disequilibrium coefficient is mostly caused by sea surface temperature (SST), if the coefficients in the equation developed by *Ciais et al.* (1995b) are assumed to be accurate. With an error of 1.0K in SST, the error in the calculated global average disequilibrium coefficient is ±0.12‰. The error in one-way the ocean flux is difficult to estimate, but we use the value of 10 PgC y^{-1} inferred from the global isotopic budget uncertainty by *Alden* et al. (2010). Their inferred range of the ocean disequilibrium flux is from 92.3 to100.2 PgC y^{-1} ‰, and we use our disequilibrium coefficient of 0.78‰ to calculate this one-way flux uncertainty. Based on the OPA-PISCES-T model, the one-way flux from ocean to atmosphere is 84.6 PgC y^{-1}, and the uncertainty in the estimated ocean disequilibrium flux is therefore ±(0.12×84.6+0.78×10) = 19.8 PgC y^{-1} ‰.

Case III, Case IV and Case V are conducted to investigate the sensitivity of the inverted carbon flux to the disequilibrium fluxes over land and ocean (Table 3). In Case III, where the disequilibrium over land is ignored while other settings remain the same as Case I, the land sink increases by 1.03 PgC y^{-1}, while the ocean sink increases by 0.09 PgC y^{-1} in comparison with Case I. When the disequilibrium over ocean is ignored instead (Case IV), the land sink increases by 0.09 PgC y^{-1}, while the ocean sink increases by 2.21 PgC y^{-1}, in comparison with Case I. When the disequilibria over both land and ocean are ignored, the land sink increases by 1.12 PgC y^{-1}, while the ocean sink increases by 2.21 PgC y^{-1}, in comparison with Case I. Results from these case studies suggest that in the joint inversion using both CO_2 and $^{13}CO_2$ measurements, the inverted CO_2 flux can be significantly influenced by the disequilibrium fluxes of land and ocean. The carbon sinks over land and ocean increase when these disequilibrium fluxes are ignored because the photosynthetic and diffusive sources of $^{13}CO_2$ have to increase to make up for the shortfall due to ignoring the disequilibrium sources. These pronounced influences of the disequilibrium fluxes on the CO_2 sink inversion suggest that $^{13}CO_2$ data contain strong signals for the global carbon cycle. In the joint inversion, these data can have the power to distort the global CO_2 mass balance if the $^{13}CO_2$ mass budget (Eq. 8) is not properly simulated.

The impacts of these disequilibrium fluxes on the inverted CO_2 flux determined in Case III, Case IV and Case V are similar to previous results using the double deconvolution technique (*Tans et al.*, 1993; *Ciais et al.*, 1995b*; Randerson et al.*, 2002). However, the influences of the these disequilibrium fluxes on the joint inversion could possibly be compromised due to the small number of ^{13}C observation sites relative to the number of CO_2 observation sites used in the joint inversion. The number of linear equations for CO_2 concentration in our joint inversion system (Eq. 6) greatly exceeds the number for ^{13}C composition, with a potential of dampening the impact of ^{13}C data on the inverted results. To investigate the possibility of this dampening effect, we conducted a set of inversions using ^{13}C data alone (Table 6) and found that the impacts of the disequilibrium fluxes on the inversion results are similar to those of the joint inversion. In Case V shown in Table 4, for

Geosci. Model Dev. Discuss., doi:10.5194/gmd-2016-53, 2016
Manuscript under review for journal Geosci. Model Dev.
Published: 17 May 2016

example, ignoring the disequilibrium fluxes causes the land sink to increase by 1.06 PgC y^{-1} and ocean sink to increase by 2.31 PgC y^{-1}, resulting in a total increase of 3.37 PgC y^{-1}, which is similar to the total difference of 3.33 PgC y^{-1} produced by the joint inversion. These similar results suggest that ^{13}C data used in the way described by Eqs. 6-8 have played the expected role in the joint inversion. By comparing results shown in Tables 3 and 6, it is also encouraging to see that inversions using ^{13}C data alone can produce reasonable results for the CO_2 flux, although we believe that the joint inversion results shown in Table 3 are more reliable.

According to the sensitivity of the inverted flux to the land disequilibrium flux found in comparison of Case III to Case I, the uncertainty of 11.2 PgC y^{-1} ‰ in the land disequilibrium flux would cause an uncertainty of 0.47 PgC y^{-1} in the land flux, assuming the sensitivity is linear. According to the comparison between Case IV to Case I, the uncertainty of 16.3 PgC y^{-1} ‰ in the ocean disequilibrium flux would cause an uncertainty of 0.54 PgC y^{-1} in the ocean flux. These uncertainties in the land and ocean fluxes are 17% and 24% of the jointly inverted fluxes for land and ocean (Case I in Table 3), respectively. The impact of the uncertainty in the disequilibrium flux over land is only slightly smaller than the posterior uncertainty of the inverted land flux, but the impact over ocean is larger than the posterior uncertainty.

4. Discussion

After the CO_2 fluxes are optimized through the inversions, the posterior CO_2 concentration at all stations in each month can be calculated from Eq. 2, and similarly the posterior $^{13}CO_2$ composition can also be calculated from Eq. 10 by replacing the prior discrimination fluxes with posterior discrimination fluxes. One way to evaluate the effectiveness of the joint inversion is to examine the improvement in the posterior CO_2 and $^{13}CO_2$ concentrations against measurements. Figure 13 shows concentrations for 10 randomly selected stations from different regions, which are indicated in Figure 1. The CO_2 and $^{13}CO_2$ concentrations produced using the prior fluxes considerably deviate from observations at all stations. The posterior CO_2 concentration from the CO_2-only inversion shows great improvements over the prior concentration in comparison with observations. The posterior CO_2 concentration from the joint inversion does not differ significantly from that of the CO_2-only inversion. At some stations the joint inversion produces slightly lower root mean square differences (RMSD) against observations, but in some stations the opposite is true, as indicated by the RMSD values shown in the header of each plot. It is expected that in some stations, the posterior CO_2 concentration in the joint inversion can be slightly worsened because of the influence of $^{13}CO_2$. The posterior $^{13}CO_2$ concentration is pronouncedly improved over the prior in comparison with observations and almost mimics the observed magnitudes and temporal variations, indicating the joint inversion system can forcefully adjust CO_2 fluxes to match with $^{13}CO_2$ observation through the prescribed discrimination rates. In order to provide a comprehensive evaluation, the posterior CO_2 and $^{13}CO_2$ concentrations at all stations are shown in Figures 14 and 15 against observations. In Figure 14, we see pronounced improvements in the posterior concentrations from both the CO_2-only and joint inversions over the prior case. However, the improvements of these two inversions are similar (the joint inversion has a smaller intercept and a slope closer to one, but the CO_2-only inversion has a slightly larger r^2 value). This is in agreement with the cases shown for the individual stations: some stations are improved and some worsened by the use of $^{13}CO_2$ data, manifesting the force of this additional data on the inversion. In Figure 15, the posterior $^{13}CO_2$

Geosci. Model Dev. Discuss., doi:10.5194/gmd-2016-53, 2016
Manuscript under review for journal Geosci. Model Dev.
Published: 17 May 2016

concentration from the joint inversion is shown to be greatly improved from the prior case. In the joint inversion, the increase of the posterior land and ocean sinks over the prior sinks that remove CO_2 from the atmosphere logically corrects for the positive bias in the CO_2 concentration produced using the prior fluxes (Figure 14a). The posterior concentration correlation with observation is stronger for $^{13}CO_2$ than for CO_2, indicating that isofluxes are effectively optimized in the joint inversion according to $^{13}CO_2$ data. However, some points in Figure 15b scatter greatly from the 1:1 line, and these points are mostly likely the missing data filled with the reference data (Section 2.4). As other error sources cannot be excluded, these data are retained in our inversion.

After adding $^{13}CO_2$ data to the inversion system, the uncertainty in the inverted CO_2 flux reduced from 0.84 to 0.76 PgC y^{-1} for land and from 0.40 to 0.35 PgC y^{-1} for ocean (Table 3, difference between the CO_2-only case and Case I), i.e. 9% and 13% reductions in uncertainty for land and ocean, respectively. In the joint inversion, the relative error in $^{13}CO_2$ measurements is similar to that in CO_2 measurement and the uncertainty in the prior $^{13}CO_2$ flux estimation is not required, and therefore the posterior uncertainty in the inverted CO_2 flux does not directly take into account of the error in the prior $^{13}CO_2$ flux estimation. However, through the use of modeled photosynthetic discrimination and the disequilibrium fluxes over land and ocean, the prior $^{13}CO_2$ flux estimation has influence on the inversion results. Errors in modeling the spatial and temporal variations of the $^{13}CO_2$ flux stem from many sources including errors in modeling the discrimination, which is affected by the fractionation of the $^{13}CO_2$ flow through leaf boundary layer, stomata, mesophyll, etc., and the disequilibrium, which depends on the sizes of 9 soil carbon pools and their ages. Although the ocean $^{13}CO_2$ discrimination is small, its disequilibrium has a strong latitudinal gradient, which is approximately calculated using the mean monthly temperature. The error in the calculated ocean disequilibrium coefficient is estimated to be±1.2‰ for the monthly values at a given location and ±0.12‰ for the global annual total. Because of these errors, we estimate that the relative uncertainty in the prior $^{13}CO_2$ fluxes is similar to that of the prior CO_2 flux over both land and ocean.

5. Conclusion

The usefulness of atmospheric $^{13}CO_2$ measurements at 73 stations for global carbon cycle estimation is explored through their use as an additional constraint on an atmospheric inversion of the surface carbon flux using CO_2 observations. The following conclusions are drawn from this study:

1. This ^{13}C constraint on the joint inversion considerably alters the partition between land and ocean sinks obtained from CO_2-only inversion, decreasing the land sink from 3.40±0.84 to 2.78±0.76 Pg C y^{-1}, while increasing the ocean sink from 1.48±0.40 to 2.26±0.35 Pg C y^{-1} for the 2002-2004 period. Over land, this alteration induces the largest sink increases in the Amazon region and largest source increases in southern Africa and Asia, where CO_2 observations are sparse and therefore the additional signal from $^{13}CO_2$ data becomes most important. Over ocean, sink increases are found broadly at middle and high latitudes in both hemispheres.

Geosci. Model Dev. Discuss., doi:10.5194/gmd-2016-53, 2016
Manuscript under review for journal Geosci. Model Dev.
Published: 17 May 2016

2. The spatial distribution of the $^{13}CO_2$ discrimination rate over land has considerable impacts on the spatial distribution of the inverted CO_2 sink over land (up to 15% in some regions), suggesting that reliable models for simulating the spatial distribution of the ^{13}C discrimination rate over land are needed for effective use of $^{13}CO_2$ data for global carbon cycle inversion.

3. The joint inversion is sensitive to the $^{13}CO_2$ disequilibrium fluxes over both land and ocean. Ignoring these fluxes in the joint inversion causes the inverted total land and ocean sink to increase by 1.03 and 2.21 PgC y^{-1}, respectively. The uncertainty in our disequilibrium flux calculation is estimated to be 11.2 PgC y^{-1} ‰ and 16.3 Pg C y^{-1} ‰ for land and ocean, respectively, inducing an uncertainty in the inverted flux of 0.47 Pg C y^{-1} for land and 0.54 Pg C y^{-1} for ocean.

6. Code and Data Availability

The inversion code and data, including processed CO_2 and $^{13}CO_2$ data as inputs to the inversion system, prior land and ocean CO_2 fluxes, and prior $^{13}CO_2$ disequilibrium and discrimination fluxes over land and ocean, will be available publically after this manuscript is accepted for publication. The contact is Mr. Gang Mo, gangmo@geog.utoronto.ca, and the data depository will be http://faculty.geog.utoronto.ca/Chen/webdata/data/inversion.

7. Acknowledgement

We greatly appreciate the GlobalView dataset that is available from the NOAA Climate Monitoring and Diagnostics Laboratory. NCEP/DOE 2 Reanalysis data are provided by the NOAA/OAR/ESRL PSD, Boulder, Colorado, USA, from their Web site at http://www.esrl.noaa.gov/psd/. This research was support by a grant (2010CB950704) from the Global Change Key Program of the Chinese Ministry of Science and Technology and a grant (GR-646) from the former Canadian Foundation for Climate and Atmospheric Sciences. Drs. Misa Ishizawa, Douglas Chan and Kaz Higuchi of Environment Canada (EC) provided useful suggestions and technical assistance at the beginning of the project, and Jonathan Fung assisted in the CO_2-only inversion during his M.Sc. studies. We are also indebted to Drs. Pieter Tans of NOAA and Lin Huang of EC for their guidance in the development and validation of the isotope module in BEPS in the early years.

8. References

Alden, C., J. B. Miller, and J. W. C. White (2010), Can bottom-up ocean CO2 fluxes can be reconciled with atmospheric 13C observations?, *Tellus B*, 62B, 369-388.

Andres R.J., G. Marland, T. Boden T., and S. Bischof (2000), Carbon dioxide emissions from fossil fuel consumption and cement manufacture, 1751-1991, and an estimate of their isotopic composition and latitudinal distribution, in Wigley T.M.L., Schimel D.S. (eds.) *The Carbon Cycle*. Cambridge: Cambridge University Press. 53-62.

Aumont, O., E. Maier-Reimer, S. Blain, and P. Monfray (2003), An ecosystem model of the global ocean including Fe, Si, P colimitations, *Global Biogeochem. Cycles*, *17*(2), 1060.

Baker, D. F., R. M. Law, K. R. Gurney, P. Rayner, P. Peylin, A. D. Denning, P. Bousquet, L. Bruhwiler, Y. H. Chen, P. Ciais, I. Y. Fung, M. Heimann, J. John, T. Maki, S. Maksyutov, K. Masarie, M. Prather, B. Pak, S. Taguchi, and Z. Zhu (2006), TransCom 3 inversion intercomparison: Impact of transport model errors on the interannual variability of regional CO2 fluxes, 1988–2003, Global Biogeochem. Cy., 20, GB1002, doi:10.1029/2004GB002439.

Ball, J. T. (1988), An analysis of stomatal conductance, Ph.D. thesis, 89 pp., Stanford Univ., Stanford, Calif.

Beer, C., M. Reichstein, E. Tomelleri, P. Ciais, M. Jung, N. Carvalhais, C. Rodenbeck, M.A. Arain, D. Baldocchi, G.B. Bonan, A. Bondeau, A. Cescatti, G. Lasslop, A. Lindroth, M. Lomas, S. Luyssaert, H. Margolis, K.W. Oleson, O. Roupsard, E. Veenendaal, N. Viovy, C. Williams, F.I. Woodward, and D. Papale (2010), Terrestrial Gross Carbon Dioxide Uptake: Global Distribution and Covariation with Climate, *Science* 329:834-838.

Buitenhuis, E., C. Le Quéré, O. Aumont, G. Beaugrand, A. Bunker, A. Hirst, T. Ikeda, T. O'Brien, S. Piontkovski, and D. Straile (2006), Biogeochemical fluxes through mesozooplankton, *Global Biogeochem. Cycles*, *20*(2), GB2003.

Canadell, J. G., C. Le Quéré, M. R. Raupach, C. B. Field, E. T. Buitenhuis, P. Ciais, T. J. Conway, N. P. Gillett, R. A. Houghton, and G. Marland (2007), Contributions to accelerating atmospheric CO_2 growth from economic activity, carbon intensity, and efficiency of natural sinks, *Proceedings of the National Academy of Sciences*, *104*(47), 18866-18870.

Chen, B., J. M. Chen, P. Tabs and L. Huang (2006), Simulating dynamics of $^{13}CO_2$ in the planetary boundary layer over a boreal forest region: An approach to estimate carbon isotope rectification. *Tellus 58B*, 537-549.

Chen, B., and J. M. Chen, 2007. InterannualTemporal variation in carbon isotope discrimination in response to meteorological and physiological driving factors in a boreal forest ecosystem, *Plant, Cell and Environment*, 30: doi: 10.1111/j.1365-3040.2007.01707.

Chen, J. M., J. Liu, J. Cihlar, and M. L. Goulden (1999), Daily canopy photosynthesis model through temporal and spatial scaling for remote sensing applications, *Ecological Modelling*, *124*(2-3), 99-119.

Chen, J. M., W. Ju, J. Cihlar, D. Price, J. Liu, W. Chen, J. Pan, T. A. Black, and A. Barr (2003), Spatial distribution of carbon sources and sinks in Canada's forests based on remote sensing, *Tellus B.* 55(2): 622-642.

Chen, J. M., C. H. Menges, and S. G. Leblanc (2005), Global derivation of the vegetation clumping index from multi-angular satellite data, *Remote Sensing of Environment*, 97: 447-457.

Chen, J. M., G. Mo, J. Pisek, J. Liu, F. Deng, M. Ishizawa, and D. Chan (2012), Effects of foliage clumping on the estimation of global terrestrial gross primary productivity, *Global Biogeochem. Cycles*, 26, GB1019, doi:10.1029/2010GB003996.

Chen, J. M., J. Fung, G. Mo, F. Deng, and T. West (2015), Atmospheric inversion of the global surface carbon flux with consideration of the spatial distribution of US crop production and consumption. *Biogeosciences*, 12, 323-343.

Ciais, P., P. P. Tans, M. Trolier, J.W. C. White, and R. J. Francey (1995a). A large northern-hemisphere terrestrial CO2 sink indicated by the 13C/12C ratio of atmospheric CO2. *Science*, 269, 1098-1102.

Ciais, P., P. P. Tans, J. W. C. White, M. Trolier, R. J. Francey, J. A. Berry, D. R. Randall, P. J. Sellers, J. G. Collatz, and D. S. Schimel (1995b), Partitioning of ocean and land uptake of CO_2 as inferred by $\delta^{13}C$ measurements from the NOAA Climate Monitoring and Diagnostics Laboratory Global Air Sampling Network, *J. Geophys. Res.*, 100(D3), 5051–5070, doi:10.1029/94JD02847.

Davidson, E. A., A. C. de Araujo, P. Artaxo et al., (2012), The Amazon basin in transition. *Nature*, 481, 321-328.

Deng, F., J. M. Chen, M. Ishizawa, C.-W. Yuen, G. Mo, K. A. Z. Higuchi, D. Chan, and S. Maksyutov (2007), Global monthly CO_2 flux inversion with a focus over North America, *Tellus B*, *59*(2), 179-190.

Deng, F., J. M. Chen, S. Plummer, M. Chen, and J. Pisek (2006), Algorithm for global leaf area index retrieval using satellite imagery, *IEEE Transactions on Geoscience and Remote Sensing*, *44*(8), 2219-2229.

Deng, F., and J. M. Chen (2011), Recent global CO_2 flux inferred from atmospheric CO_2 observations and its regional analysis. *Biogeosciences*, 8: 3263–3281.

DeVries, T. (2014), The oceanic anthropogenic CO2 sink: Storage, air-sea fluxes, and transports over the industrial era, *Global Biogeochem. Cycles*, *28*, 631–647, doi:10.1002/2013GB004739.

Enting, I.G., C.M. Trudinger, R.J. Francey and H. Granek (1993), Synthesis inversion of atmospheric CO_2 using the GISS tracer transport model, *Division of Atmospheric Research technical paper*, No.29, CSIRO Australia.

Enting, I. G., C. M. Trudinger, and R. J. Francey (1995), A synthesis inversion of the concentration and $\delta^{13}C$ of atmospheric CO_2. *Tellus B*, 47: 35–52.

Enting, I. G. (2002), *Inverse Problems in Atmospheric Constituents transport*, Cambridge University Press.

Farquhar, G. D., S. von Caemmerer, and J. A. Berry (1980), A biochemical model of photosynthetic CO_2 assimilation in leaves of C3 species, *Planta*, 149, 78–90, doi:10.1007/BF00386231.

Farquhar, G. D., and R. A. Richards (1984), Isotopic composition of plant carbon correlates with water-use efficiency of wheat genotypes, *Aust., J. Plant. Physiol*., 11, 539–552.

Farquhar G.D., J. R. Ehleringer and K. T. Hubick (1989), Carbon isotope discrimination and photosynthesis. *Annual Review of Plant Physiology and Plant Molecular Biology*. 40:503–537.

Francey, R. J., P. P. Tans, C. E. Allison, I. G. Enting, J. W. C. White, and M. Trolier (1995), Changes in oceanic and terrestrial carbon uptake since 1982. *Nature*, 373, 326–330.

Francey R. J., C. E. Allison, D. M. Etheridge, C. M. Trudinger, I. G. Enting, M. Leuenberger, R. L. Langenfelds, E. Michel, L. P. Steele (1999), A 1000-year high precision record of $\delta^{13}C$ in atmospheric CO_2, *Tellus B*, 51(2), 170–193.

Fung, I.Y., C. B. Field, J. A. Berry, M. V. Thompson, J. T. Randerson, C. M. Malmström, P. M. Vitousek, G. James Collatz, P. J. Sellers, D. A. Randall, A. S. Denning, F. Badeck (1997), Carbon-13 exchanges between the atmosphere and biosphere, *Global Biogeochemical Cycles*, 11: 507-533.

Garrigues S., R. Lacaze, F. Baret, J.T. Morisette, M. Weiss, J.E. Nickeson, R. Fernandes, S. Plummer, N.V. Shabanov, R.B. Myneni, Y. Knyazikhin, W. Yang (2008), Validation and intercomparison of global Leaf Area Index products derived from remote sensing data, *J. Geophys. Res*., 113, G02028:doi:10.1029/2007JG000635.

GLOBALVIEW-CO2C13: Cooperative Atmospheric Data Integration Project - $\delta^{13}C$ of Carbon Dioxide. CD-ROM, NOAA ESRL, Boulder, Colorado [Also available on Internet via anonymous FTP to ftp.cmdl.noaa.gov, Path: ccg/co2c13/GLOBALVIEW], 2009.

Govind, A., and J. M. Chen (2011), Spatially distributed modeling of the long-term carbon balance of a boreal landscape. *Ecological Modeling*, doi:10.1016/j.ecolmodel.2011.04.007.

Gurney, K. R., R. M. Law, A. S. Denning, P. J. Rayner, D. Baker, P. Bousquet, L. Bruhwiler, Y. H. Chen, P. Ciais, S.M. Fan, I. Y. Fung, Manuel Gloor, Martin Heimann, K Higuchi, J. John, T Maki, S. Maksyutov, K. Masarie, P. Peylin, M. Prather, B. C. Pak, J. T. Randerson, J. L. Sarmiento, S. Taguchi, T Takahashi, C. W. Yuen (2002), Towards robust regional estimates of CO_2 sources and sinks using atmospheric transport models, *Nature*, *415*(6872), 626-630.

Gurney, K. R., K. R. Gurney, R. M. Law, A. S. Denning, P. J. Rayner, D. Baker, P. Bousquet, L. Bruhwiler, Y. H. Chen, P. Ciais, S.M. Fan, I. Y. Fung, M. Gloor, M. Heimann, K. Higuchi, J. John, E. Kowalczyk, T. Maki, S. Maksyutov, P. Peylin, M. Prather, B. C. Pak, J. L. Sarmiento, S. Taguchi, T. Takahashi, C. W. Yuen (2003), TransCom3 CO_2 inversion intercomparison: 1. Annual mean control results and sensitivity to transport and prior flux information, *Tellus B*, *55*(2), 555-579.

Harley, P. C., F. Loreto, G. Di Marco, and T. D. Sharkey (1992), Theoretical Considerations when Estimating the Mesophyll Conductance to CO_2 Flux by Analysis of the Response of Photosynthesis to CO_2, *Plant Physiol.* 98:1429–1436.
Houghton, R.A. (2007), Balancing the global carbon budget, *Annual Review of Earth and Planetary Sciences* 35:313-347.

Ise, T., C. M. Litton, C. P. Giardina, and A. Ito (2010), Comparison of modeling approaches for carbon partitioning: impact on estimates of global net primary production and equilibrium biomass of woody vegetation from MODIS GPP. *Journal of Geophysical Research*, Vol., 115, G04025, doi:10.1029/2010JG001326.

Jacobson, A., S. Fletcher, N. Gruber, J. Sarmiento, and M. Gloor (2007), A joint atmosphere-ocean inversion for surface fluxes of carbon dioxide: 2. Regional results, *Global Biogeochem. Cycles*, *21*(1), GB1020, doi:10.1029/2006GB002703.

Ju, W., and J. M. Chen (2005), Distribution of soil carbon stocks in Canada's forests and wetland simulated based on drainage class, topography and remote sensing. *Hydrological Processes*, 19:77-94.

Kalnay, E., M. Kanamitsu, R. Kistler, W. Collins, D. Deaven, L. Gandin, M. Iredell, S. Saha, G. White, J. Woollen, Y. Zhu, A. Leetmaa, B. Reynolds, M. Chelliah, W. Ebisuzaki, W. Higgins, J. Janowiak, K. C. Mo, C. Ropelewski, J. Wang, R. Jenne, and D. Joseph (1996), The NCEP/NCAR 40-year reanalysis project, *Bull. Amer. Meteor. Soc.*, *77*, 437-471.

Kanamitsu, M., W. Ebisuzaki, J. Woollen, S-K Yang, J. J. Hnilo, M. Fiorino, and G. L. Potter. (2002), NCEP-DEO AMIP-II Reanalysis (R-2), *Bulletin of the American Meterological Society*, 1631-1643.

Keeling, C. D., R. B. Bacastow, A. F. Carter, S. C. Piper, T. P. Whorf, and co-authors (1989a). A three-dimensional model of atmospheric CO2 transport based on observed winds: 1. analysis of observational data. In: Aspects of climate variability in the Pacific and Western Americas (ed. Peterson, D. H.). American Geophysical Union, Washington, D.C., 165-236.

Keeling, C. D., S. C. Piper, and M. Heimann (1989b). A three-dimensional model of atmospheric CO2 transport based on observed winds: 4. Mean annual gradients and interannual variations. In: Aspects of climate variability in the Pacific and Western Americas (ed. Peterson, D. H.). American Geophysical Union, Washington D.C., 305-363.

Krol, M. C., J. Lelieveld, D. E. Oram, G. A. Sturrock, S. A. Penkett, C. A. M. Brenninkmeijer, V. Gros, J. Williams, and H. A. Scheeren (2003), Continuing emissions of methyl chloroform from Europe, *Nature*, *421*(6919), 131-135.

Krol, M. C., S. Houweling, B. Bregman, M. van den Broek, A. Segers, P. van Velthoven, W. Peters, F. Dentener, and P. Bergamaschi (2005), The two-way nested global chemistry-transport zoom model TM5: algorithm and applications, *Atmos. Chem. Phys.*, *5*(2), 417-432.

Landschützer, P., N. Gruber, D. C. E. Bakker, and U. Schuster, (2014), ecent variability of the global ocean carbon sink. *Global Biogeochemical. Cycles*, *28*, 927–949, doi:10.1002/2014GB004853.

Le Quéré, C, Andres, R. J., Boden, T., Conway, T., Houghton, R. A., House, J. I., Marland, G., Peters, G. P., van der Werf G. R., Ahlstrom, A., Andrew, R. M., Bopp, L., Canadell, J. G., Ciais, P., Doney, S. C., Enright, C., Friedlingstein, P., Huntingford, C., Jain, A. K., Jourdain, C., Kato, E., Keeling, R. F., Klein G. K., Levis, S., Levy, P., Lomas, M., Poulter, B., Raupach, M. R., Schwinger, J., Sitch, S., Stocker, B. D., Viovy, N., Zaehle. S., and Zeng. N. (2013). The global carbon budget 1959–2011. ***Earth Syst. Sci. Data*** 5: 165–185, doi:10.5194/essd-5-165-2013.

Liu, J., J. M. Chen, J. Cihlar, and W. M. Park (1997), A process-based boreal ecosystem productivity simulator using remote sensing inputs, *Remote Sensing of Environment*, *62*(2), 158-175.

Madec, G., P. Delecluse, M. Imbard, and C. Lévy (1998), OPA 8.1 ocean general circulation model reference manual, *Notes du pôle de modélisation IPSL*, 91pp, http://www.lodyc.jussieu.fr/opa/.

Majkut, J. D., J. L. Sarmiento, and K. B. Rodgers (2014), A growing oceanic carbon uptake: results from an inversion study of surface pCO2 data. *Global Biogeochemical Cycles*, *28*, 335–351, doi:10.1002/2013GB004585.

Marland, G., T. A. Boden, and R. J. Andres (2009), Global, Regional, and National Fossil Fuel CO_2 Emissions. In Trends: A Compendium of Data on Global Change. Carbon Dioxide Information Analysis Center, Oak Ridge National Laboratory, U.S. Department of Energy, Oak Ridge, Tenn., U.S.A.

Masarie, K. A., and P. P. Tans (1995), Extension and integration of atmospheric carbon dioxide data into a globally consistent measurement record, *J. Geophys. Res*., 100(D6), 11593-11610.

Michalak, A. M., A. Hirsch, L. Bruhwiler, K. R. Gurney, W. Peters, and P. P. Tans (2005), Maximum likelihood estimation of covariance parameters for Bayesian atmospheric trace gas surface flux inversions, *J. Geophys. Res*., 110, D24107, doi:10.1029/2005JD005970.

Olivier, J. G. J., J. A. Van Aardenne, F. J. Dentener, V. Pagliari, L. N. Ganzeveld, and J. A. H. W. Peters (2005), Recent trends in global greenhouse gas emissions:regional trends 1970–2000 and spatial distributionof key sources in 2000, *Environmental Sciences*, *2*(2), 81 - 99.

Park, G. H., R. Wanninkhof, S. C. Doney, T. Takahashi, K. Lee, R. A. Feely, C. L. Sabine, J. Trinanes, and I. D. Lima, (2010), Variability of global net sea-air CO2 fluxes over the last three decades. Chemical and Physical Meteorology, 62, 352–368.

Patra, P. K., S. Maksyutov, M. Ishizawa, T. Nakazawa, T. Takahashi, and J. Ukita (2005), Interannual and decadal changes in the sea-air CO_2 flux from atmospheric CO_2 inverse modeling, *Global Biogeochem. Cycles*, *19*(4), GB4013.

Peters, W., J. B. Miller, J. Whitaker, S. A. Denning, A. Hirsch, M. Krol, D. Zupanski, L. Bruhwiler, and P. P. Tans (2005), An ensemble data assimilation system to estimate CO2 surface fluxes from atmospheric trace gas observations, J. Geophys. Res., 110, D24304, doi:10.1029/2005JD006157.

Peters, W. A. R. Jacobson, C. Sweeney, A. E. Andrews, T.J. Conway, K. Masarie, J. B. Miller, L. M. P. Bruhwiler, G. Petron, A. I. Hirsch, D. E. J. Worthy, G.R Werf, J. T. Randerson, P. O. Wennberg, M.C. Krol, P. P. Tans (2007), An atmospheric perspective on North American carbon dioxide exchange: CarbonTracker, *Proceedings of the National Academy of Sciences*, *104*(48), 18925-18930.

Peylin, P., P. Bousquet, C. Le Quéré, S. Sitch, P. Friedlingstein, G. McKinley, N. Gruber, P. Rayner, and P. Ciais (2005), Multiple constraints on regional CO_2 flux variations over land and oceans. *Global Biogeochemical Cycles* 19: doi: 10.1029/2003GB002214.

Pickett-Heaps, C. A. (2007), Atmospheric CO_2 inversion cross-validation using non-surface CO_2 data., *PhD dissertation*.

Potter, C.S., J.T. Randerson, C.B., Field, P.A. Matson, P.M. Vitousek, H.A. Mooney, and S.A. Klooster (1993), Terrestrial ecosystem production: A process model based on global satellite and surface data, *Global Biogeochemical Cycles*,7 , 811-841.

Potter, C., S. Klooster, A. Huete, V. Genovese, M. Bustamante, L. Guimaraes Ferreira, R. C. de Oliveira Jr., and R. Zepp, (2009), Terrestrial carbon sinks in the Brazilian Amazon and Cerrado region predicted from MODIS satellite data and ecosystem modeling. Biogeosciences, 6, 937–945.

Randerson, J. T., G. J. Collatz, J. E. Fessenden, A. D. Munoz, C. J. Still, J. A. Berry, I. Y. Fung, N. Suits, and A. S. Denning (2002), A possible global covariance between terrestrial gross primary production and ^{13}C discrimination: Consequences for the atmospheric ^{13}C budget and its response to ENSO, *Global Biogeochem. Cycles*, 16(4), 1136, doi:10.1029/2001GB001845

Randerson, J. T., G. R. van der Werf, L. Giglio, G. J. Collatz, and P. S. Kasibhatla (2007), Global Fire Emissions Database, Version 2 (GFEDv2.1). Data set. , *Available on-line [http://daac.ornl.gov/] from Oak Ridge National Laboratory Distributed Active Archive Center, Oak Ridge, Tennessee, U.S.A.*

Rayner, P. J, 2001. Atmospheric perspectives on the ocean carbon cycle. In E. D. Schulze, S. P. Harrison, M. Heimann, E. A. Holland, J. Lloyd, I. C. Prentice, and D. Schimel, editors, Global biogeochemical cycles in the climate system, pages 285–294. Academic Press, San Diego.

Rayner, P. J., I. G. Enting, R. J. Francey, and R. L. Langenfelds (1999), Reconstructing the recent carbon cycle from atmospheric CO_2, $\delta^{13}C$ and O_2/N_2 observations, Tellus, Ser. B, 51, 213– 232.

Rayner, P. J., R. M. Law, C. E. Allison, R. J. Francey, C. M. Trudinger, and C. Pickett-Heaps (2008), Interannual variability of the global carbon cycle (1992–2005) inferred by inversion of atmospheric CO_2 and $\delta\ ^{13}CO_2$ measurements, *Global Biogeochem. Cycles*, 22, GB3008, doi:10.1029/2007GB003068.

Reynolds, R. W and T. M. Smith (1994), Improved global sea surface temperature analyses using optimum interpolation. *J. Climate*, 7, 929–948.

Reynolds, R. W., N. A. Rayner, T. M. Smith, D. C. Stokes and W. Wang (2002), An improved in situ and satellite SST analysis for climate. *J. Climate*, 15, 1609-1625.

Richey, J. E., Melack, J. M., Aufdenkampe, A. K., Ballester, V. M. & Hess, L. L. (2002), Outgassing from Amazonian rivers and wetlands as a large tropical source of atmospheric CO2. Nature 416, 617–620.

Rödenbeck, C., S. Houweling, M. Gloor, and M. Heimann (2003), CO_2 flux history 1982-2001 inferred from atmospheric data using a global inversion of atmospheric transport, *Atmos. Chem. Phys.*, *3*(6), 1919-1964.

Rödenbeck, C., D. C. E. Bakker, N. Metzl, A. Olsen, C. Sabine, N. Cassar, F. Reum, R. F. Keeling, and M. Heimann, (2014), Interannual sea–air CO2 flux variability from an observation-driven ocean mixed-layer scheme, Biogeosciences Discuss., 11, 3167– 3207, doi:10.5194/bgd-11-3167-2014.

Scholze, M., P. Ciais, and M. Heimann (2008), Modeling terrestrial ^{13}C cycling: Climate, land use and fire, *Global Biogeochem. Cycles*, 22, GB1009, doi:10.1029/2006GB002899.

Siegenthaler, U. and H. Oeschger (1987). Biospheric CO2 emissions during the past 200 years reconstructed by deconvolution of ice core data. *Tellus* 39B, 140-154.

Sprintsin, M., J. M. Chen, and P. Czurylowicz (2011), Combining land surface temperature and shortwave infrared reflectance for early detection of mountain pine beetle infestations in western Canada. *Journal of Applied Remote Sensing* 5(1), 053566.

Steinkamp, K., and N. Gruber (2013), A joint atmosphere-ocean inversion for the estimation of seasonal carbon sources and sinks, *Global Biogeochem. Cycles*, *27*, doi:10.1002/gbc.20064.

Stephens, B., et al. (2007), Weak northern and strong tropical land carbon uptake from vertical profiles of atmospheric CO2, *Science*, *316*(5832), 1732–1735.

Suits, N. S., A. S. Denning, J. A. Berry, C. J. Still, J. Kaduk, J. B. Miller, and I. T. Baker (2005), Simulation of carbon isotope discrimination of the terrestrial biosphere, *Global Biogeochem. Cycles*, 19, GB1017, doi:10.1029/2003GB002141.

Still, C. J., J. A. Berry, G. J. Collatz, and R. S. DeFries (2003), Global distribution of C3 and C4 vegetation: Carbon cycle implications, *Global Biogeochem. Cycles*, 17(1), 1006, doi: 10.1029 / 2001 GB001807.

Tans, P. P., I. Y. Fung, and T. Takahashi (1990), Observational Contrains on the Global Atmospheric CO_2 Budget, *Science*, *247*(4949), 1431-1438.

Tans, P. P., J. A. Berry, and R. F. Keeling (1993), Oceanic ^{13}C data: A new window on CO_2 uptake by the oceans, *Global Biogeochem. Cycles*, 7, 353-368.

Tarantola, A. (1987), *Inverse Problem Theory*, 605 pp., Elsevier, Amsterdam, The Netherlands.

van der Velde, I. R., J. B. Miller, K. Schaefer, K. A. Masarie, S. Denning, J. W. C. White, P. P. Tans, M. C. Krol, and W. Peters (2013), Biosphere model simulations of interannual variability in terrestrial 13C/12C exchange, *Global Biogeochemical Cycles*, 27, 637–649.

van der Werf, G. R., J. T. Randerson, L. Giglio, G. J. Collatz, P. S. Kasibhatla, and A. F. Arellano Jr. (2006), Interannual variability of global biomass burning emissions from 1997 to 2004, *Atmos. Chem. Phys. Discuss.*, *6*(2), 3175-3226.

Webb, R. S., C. E. Rosenzweig, and E. R. Levine (1991), A global data set of soil particle size properties, *NASA Tech. Memo*., TM-4286, 40 pp.

Wanninkhof, R., G. -H. Park, T. Takahashi, C. Sweeney, R. Feely, Y. Nojiri, N. Gruber, S. C. Doney, G. A. McKinley, A. Lenton, C. Le Quéré, C. Heinze, J. Schwinger, H. Graven, and S. Khatiwala, (2013), Global ocean carbon uptake: magnitude, variability and trends, Biogeosciences, 10, 1983-2000, doi:10.5194/bg-10-1983-2013,

Zhang F., J. M. Chen, J. Chen, C. M. Gough, T. A. Martin, D. Dragoni (2012), Evaluating spatial and temporal patterns of MODIS GPP over the conterminous U.S. against flux measurements and a process model, *Remote Sensing of Environment*, Vol. 124: 717-729.

Zhang S.P., X. Yi, X. G. Zheng, Z. Q. Chen, et al., 2014. Global Carbon Assimilation System using a Local Ensemble Kalman Filter with Multiple Ecosystem Models, *Journal of Geophysical Research-Biogeosciences*, doi: 10.1002/2014JG002792.

Geosci. Model Dev. Discuss., doi:10.5194/gmd-2016-53, 2016
Manuscript under review for journal Geosci. Model Dev.
Published: 17 May 2016

Geoscientific Model Development Discussions

Table 1. Biophysical parameters are assigned by plant functional types in BEPS. References for the chosen values of these parameters are found in *Chen et al.* (2012).

Parameters *	Broadleaf Evergreen	Broadleaf Deciduous	Evergreen Conifers	Deciduous Conifers	Shrub	C4 Plants	Others
Vcmax μmol m^{-2} s^{-1} (at 25°C)	29.0±7.7	57.7±21.2	62.5±24.7	39.1±11.7	57.9±19.6	100.7±36.6	90.0±89.5
Jmax μmol m^{-2} s^{-1}	55.1	123.7	135.2	79.2	124.1	193.1	200.0
N g m^{-2}	2.17±0.8	1.74±0.71	3.10±1.35	1.81±0.64	1.86±0.84	1.62±0.61	1.69±0.69
χ_n m^2 g^{-1}	0.48	0.59	0.33	0.56	0.57	0.62	0.60
Slope (*m*)	8	8	8	8	8	4	8
Intercept (*b*), mol m^{-2} s^{-1}	0.0011	0.0011	0.0011	0.0011	0.0011	0.0011	0.0011
LAI	4.07±2.02	3.14±1.99	3.05±1.62	2.42±1.45	1.49±1.06	1.55±1.22	1.64±1.15
Clumping Index	0.66±0.045	0.70±0.047	0.74±0.057	0.78±0.051	0.75±0.059	0.75±0.050	0.76±0.059
Canopy height (m)	23	23	20	20	4	4	4

Where *V*cmax is the leaf maximum carboxylation rate at 25°C, *J*max is the maximum electron transport rate, *N* is the leaf nitrogen content, χ_n is the slope of *V*cmax variation with N, and *m* and *b* are the slope and intercept in the Ball-Berry equation. The peak growing season LAI and clumping index are given as the mean and standard deviation for each plant functional type.

Geosci. Model Dev. Discuss., doi:10.5194/gmd-2016-53, 2016
Manuscript under review for journal Geosci. Model Dev.
Published: 17 May 2016

Geoscientific Model Development Discussions

Table 2. Global average ages of soil carbon pools computed by BEPS with consideration of the influences of temperature and soil moisture on the decomposition rates of these pools.

Soil carbon pool *i*	Name	Global Average Age τ_i (yr)
1	Surface structural leaf litter	5.0
2	Surface metabolic leaf litter	2.3
3	Soil structural litter	4.4
4	Soil metabolic litter	2.3
5	Woody litter	34.9
6	Surface microbe	11.1
7	Soil microbe	28.5
8	Slow carbon	35.5
9	Passive carbon	667.9

Geosci. Model Dev. Discuss., doi:10.5194/gmd-2016-53, 2016
Manuscript under review for journal Geosci. Model Dev.
Published: 17 May 2016

Geoscientific Model Development Discussions

Table 3. Inverted fluxes (Pg C y^{-1}), averaged for 2002 –2004, for land and ocean regions with (CO_2 + $^{13}CO_2$) and without (CO_2 only) ^{13}C constraint. The negative sign denotes the flux from the atmosphere to the surface (sink). Various treatments are made to ^{13}C discrimination and disequilibrium fluxes represented by the following cases:

Case I: Full consideration of the regional differences in discrimination and disequilibrium;

Case II: Same as Case I, but the annual photosynthetic discrimination ratio is set at a constant of -14.1‰, although it's monthly variation pattern as modeled by BEPS is retained;

Case III: Same as Case I, but the disequilibrium flux over land is ignored;

Case IV: Same as Case I, but the disequilibrium flux over ocean is ignored;

Case V: Same as Case I, but the disequilibrium flux over both land and ocean is ignored.

Region	Prior flux	Double De-convolution	Inverted CO_2 flux					
			CO_2 data	CO_2 + $^{13}CO_2$ data				
				Case I	Case II	Case III	Case IV	Case V
Land	-2.61 ±2.07	2.90	-3.40 ±0.84	-2.78 ±0.76	-2.72 ±0.77	-3.82 ±0.76	-2.87 ±0.76	-3.90 ±0.76
Ocean	-2.13 ±0.67	2.36	-1.48 ±0.40	-2.26 ±0.35	-2.23 ±0.34	-2.17 ±0.35	-4.47 ±0.35	-4.38 ±0.35

Geosci. Model Dev. Discuss., doi:10.5194/gmd-2016-53, 2016
Manuscript under review for journal Geosci. Model Dev.
Published: 17 May 2016

Geoscientific Model Development Discussions

Table 4. Comparison of land and ocean disequilibrium coefficients and disequilibrium fluxes calculated in this study with those in previous studies.

Studies	Year	Land Disequilibrium Coefficient (‰)	Land Disequilibrium Flux (PgC y^{-1} ‰)	Ocean Disequilibrium Coefficient (‰)	Ocean Disequilibrium Flux (PgC y^{-1} ‰)
This study	2002-2004	0.49	26.8	0.78	66
Fung et al. (1997)	1988	0.33	N/A	N/A	N/A
Randerson et al. (2002)	1981-1994	0.33	20	0.6	55
Alden et al. (2010)	1991-2007	0.45-0.61	22.7-30.6	N/A	92.3-100.2 (globe total)
Van der Velde et al. (2013)	1991-2007	0.486	25.4	N/A	48.7
Francey et al. (1995)	1987	0.43	25.8	0.48	43.8

Geosci. Model Dev. Discuss., doi:10.5194/gmd-2016-53, 2016
Manuscript under review for journal Geosci. Model Dev.
Published: 17 May 2016

Geoscientific Model Development Discussions

Table 5. Global isotopic mass budgets averaged for the 2002-2004 period for the prior, double de-convolution, CO_2-only inversion, and joint inversion (unit: Pg C y^{-1} ‰). Also shown are ocean and land net fluxes (unit Pg C y^{-1}) for these cases for comparison purposes. For the prior fluxes, the component of each flux are indicated in the brackets. The isotopic coefficients are same among the cases.

Isotopic terms	**Prior**	**Double de-convolution**	**CO_2 –only inversion**	**Joint inversion**
$-C_a\, d(\delta_a)/dt$	15.0 [750 Pg C×(-0.02‰ y^{-1})]	15.0	15.0	15.0
$F_f\,(\,\delta_f\, - \delta_a)$*	-153.7 [8.9 Pg C y^{-1}×(-17.27‰)]	-153.7	-153.7	-153.7
$-(F_{lph}\, - F_{lb})\varepsilon_{lh}$	36.7 [2.6 Pg C y^{-1}×(-14.10‰)]	40.9	47.9	39.5
$F_{lb}(\delta_{lb}\, - \delta_{lbe})$	26.8 [54.7 Pg C y^{-1}×(-0.49‰)]	26.8	26.8	26.8
$-(F_{ao}\, - F_{oa})\varepsilon_{ao}$	4.2 [2.1 Pg C y^{-1}×(-2.00‰)]	4.8	3.0	4.6
$F_{oa}\,(\delta^e_{oa} - \delta_{oa})$	66.0 [84.6 Pg C y^{-1}×(-0.78‰)]	66.0	66.0	66.0
Global Budget	-5.0	0.8	-5.0	1.8
$(F_{lph}\, - F_{lb})$, Pg C y^{-1}	-2.6	-2.9	-3.4	-2.8
$(F_{ao}\, - F_{oa})$, Pg C y^{-1}	-2.1	-2.4	-1.5	-2.3

*F_f is the carbon emission from fossil fuel and biomass burning, 6.9 and 2.1, Pg C y^{-1}, respectively, and δ_f is weighted average 13C composition for fossil fuel and biomass burning, being 25.27‰, and δ_a=-8.0‰.

Geosci. Model Dev. Discuss., doi:10.5194/gmd-2016-53, 2016
Manuscript under review for journal Geosci. Model Dev.
Published: 17 May 2016

Geoscientific Model Development Discussions

Table 6. Inverted fluxes (Pg C y^{-1}), averaged for 2002 –2004, for land and ocean regions using ^{13}C data only. The negative sign denotes the flux from the atmosphere to the surface (sink). Various treatments are made to ^{13}C discrimination and disequilibrium fluxes represented by the cases outlined in Table 3.

5

Region	Prior flux	Inverted CO_2 flux				
		$^{13}CO_2$ data				
		Case I	Case II	Case III	Case IV	Case V
Land	-2.61 ±2.07	-2.84 ±0.77	-2.80 ±0.77	-3.85 ±0.77	-2.88 ±0.77	-3.89 ±0.77
Ocean	-2.13 ±0.67	-2.21 ±0.36	-2.21 ±0.36	-2.21 ±0.36	-4.53 ±0.36	-4.53 ±0.36

Geosci. Model Dev. Discuss., doi:10.5194/gmd-2016-53, 2016
Manuscript under review for journal Geosci. Model Dev.
Published: 17 May 2016

Figures

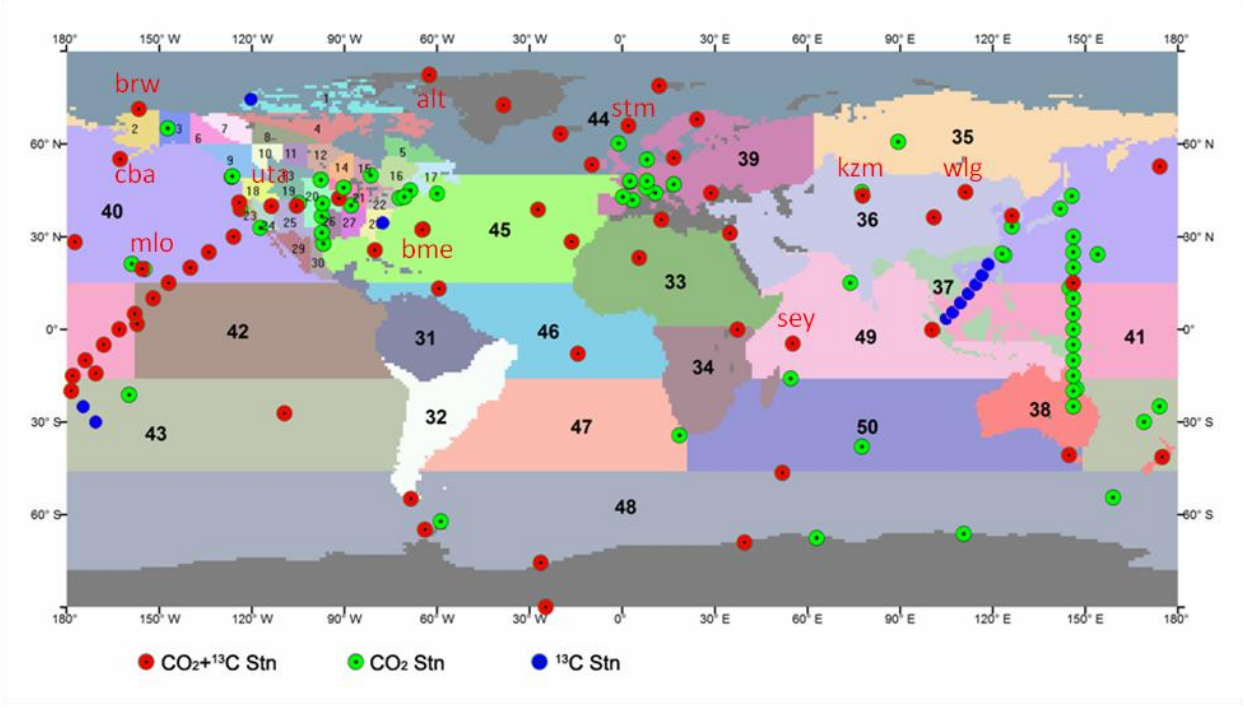

Figure 1. A global nested inversion system with a focus in North America, in which oceans are divided into 11 regions and land areas are divided into 9 large and 30 small regions outside and within North America, respectively. Also shown are CO_2 and $^{13}CO_2$ observation stations included in the GlobalView database and used in this study. 10 of the stations are marked with their names because they are selected to compare prior and posterior concentrations in Figure 11.

Geosci. Model Dev. Discuss., doi:10.5194/gmd-2016-53, 2016
Manuscript under review for journal Geosci. Model Dev.
Published: 17 May 2016

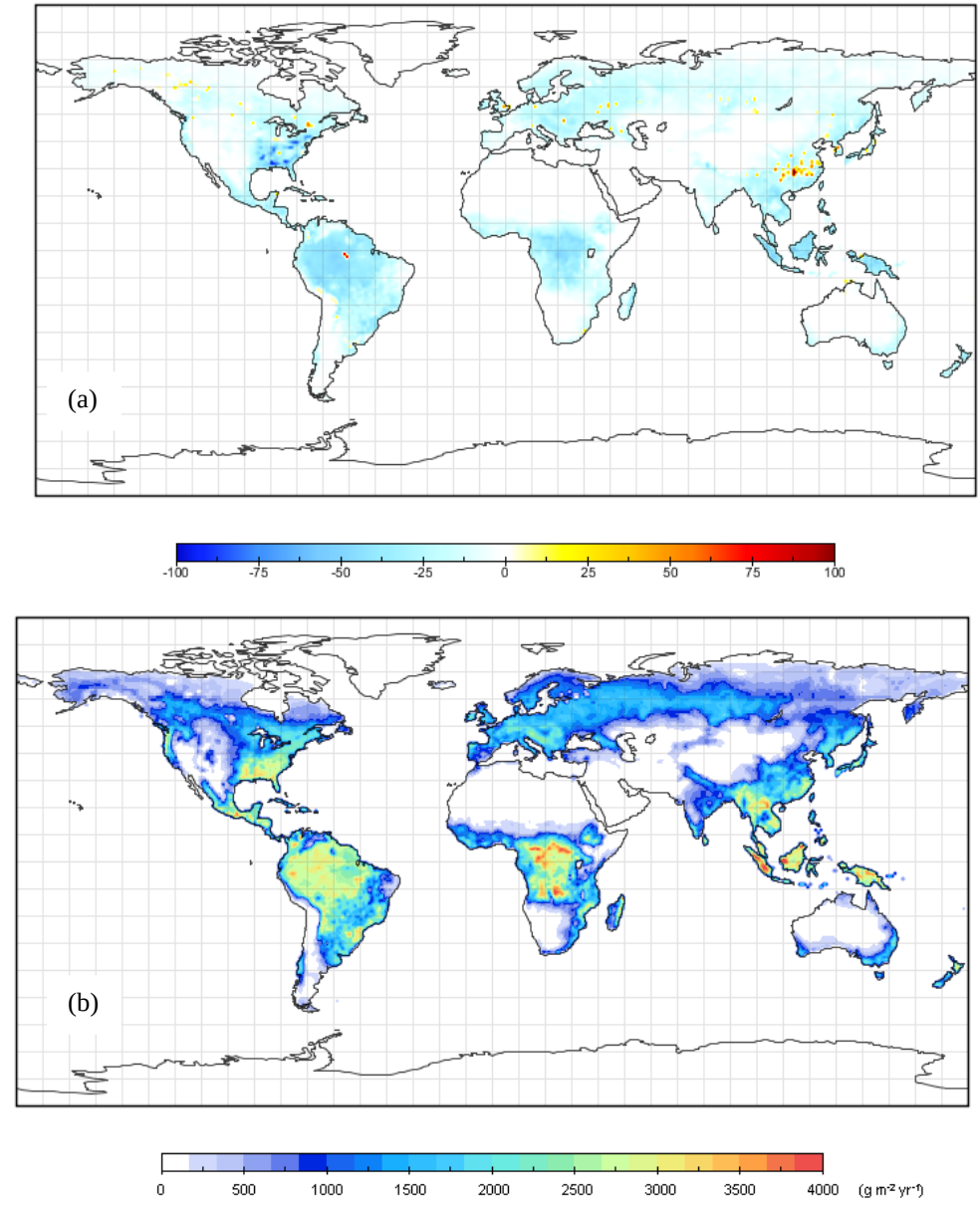

Figure 2. (a) gross primary productivity (GPP) distribution in 2003 computed using remote sensing LAI and land cover maps and climate and soil data, and (b) net ecosystem productivity (NEP) distribution in 2003. Both are calculated using the BEPS model. Annual NEP maps from 2000 to 2004 are used to as the prior flux in the inversions. This GPP map is used to distribute the flux uncertainty among the 39 land regions.

Geosci. Model Dev. Discuss., doi:10.5194/gmd-2016-53, 2016
Manuscript under review for journal Geosci. Model Dev.
Published: 17 May 2016

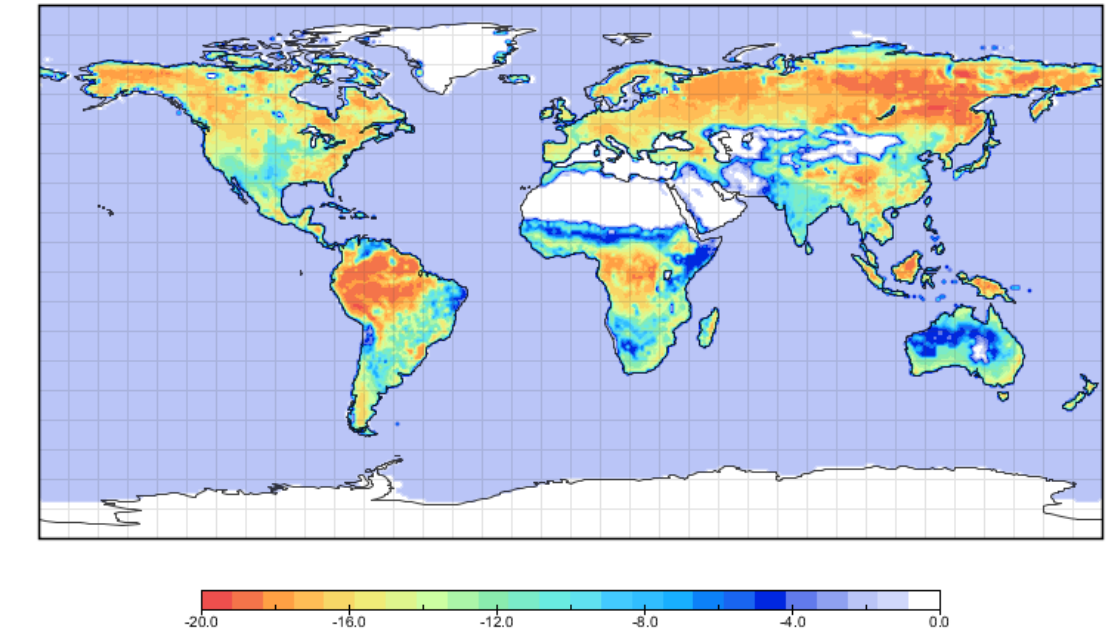

Figure 3. The annual mean of the total photosynthetic ^{13}C discrimination (Δ in Eq. 7) in 2003.

Geosci. Model Dev. Discuss., doi:10.5194/gmd-2016-53, 2016
Manuscript under review for journal Geosci. Model Dev.
Published: 17 May 2016

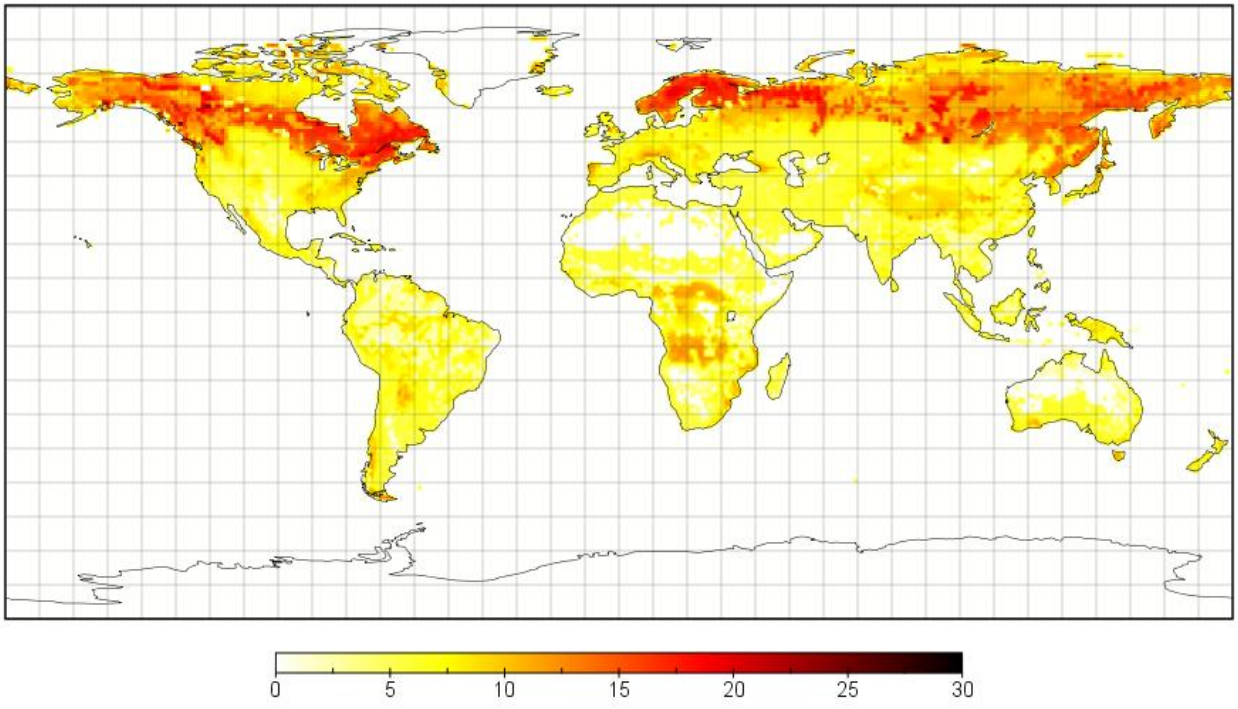

Figure 4. Global distribution of the flux-weighted mean age of soil carbon pools (Eq. 8).

Geosci. Model Dev. Discuss., doi:10.5194/gmd-2016-53, 2016
Manuscript under review for journal Geosci. Model Dev.
Published: 17 May 2016

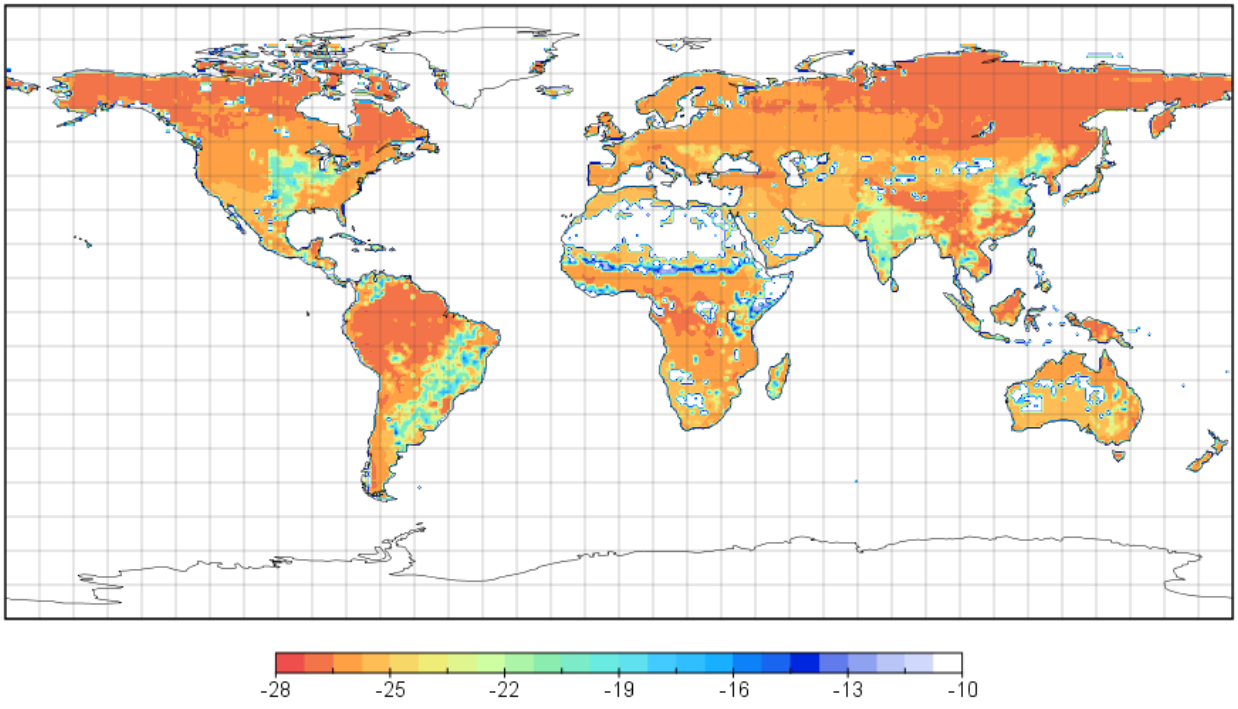

Figure 5. Global $\delta^{13}C$ distribution over land (annual flux-weighted average in 2003).

Geosci. Model Dev. Discuss., doi:10.5194/gmd-2016-53, 2016
Manuscript under review for journal Geosci. Model Dev.
Published: 17 May 2016

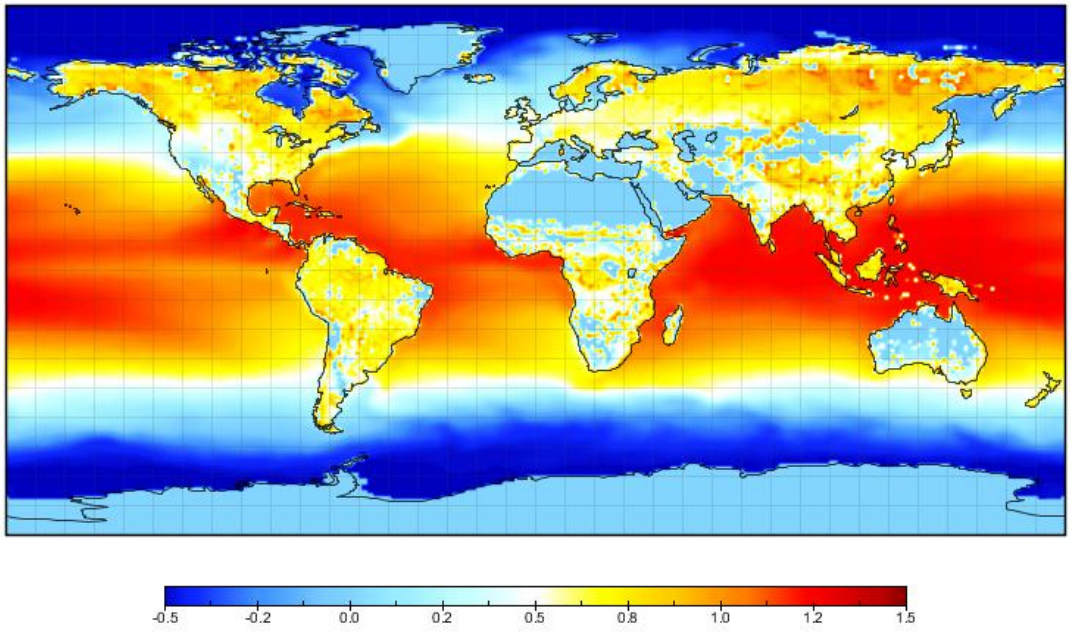

Figure 6. Disequilibria between ^{13}C fluxes to and from the land or ocean surface in 2000. At the land surface, the disequilibrium is the difference between photosynthetic and respiratory discriminations against ^{13}C, and at the ocean surface, it is the difference in ^{13}C discrimination between the one-way diffusive downward and upward fluxes.

Geosci. Model Dev. Discuss., doi:10.5194/gmd-2016-53, 2016
Manuscript under review for journal Geosci. Model Dev.
Published: 17 May 2016

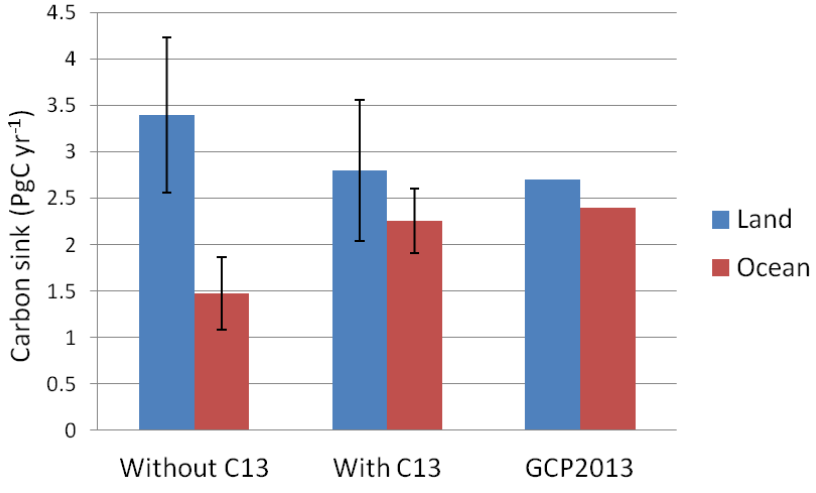

Figure 7. Comparison of land and ocean carbon sinks derived from inversions with and without the $^{13}CO_2$ constraint against the Global Carbon Project results (*Le Quéré et al.*, 2013).

Geosci. Model Dev. Discuss., doi:10.5194/gmd-2016-53, 2016
Manuscript under review for journal Geosci. Model Dev.
Published: 17 May 2016

Geoscientific Model Development Discussions
Open Access
EGU

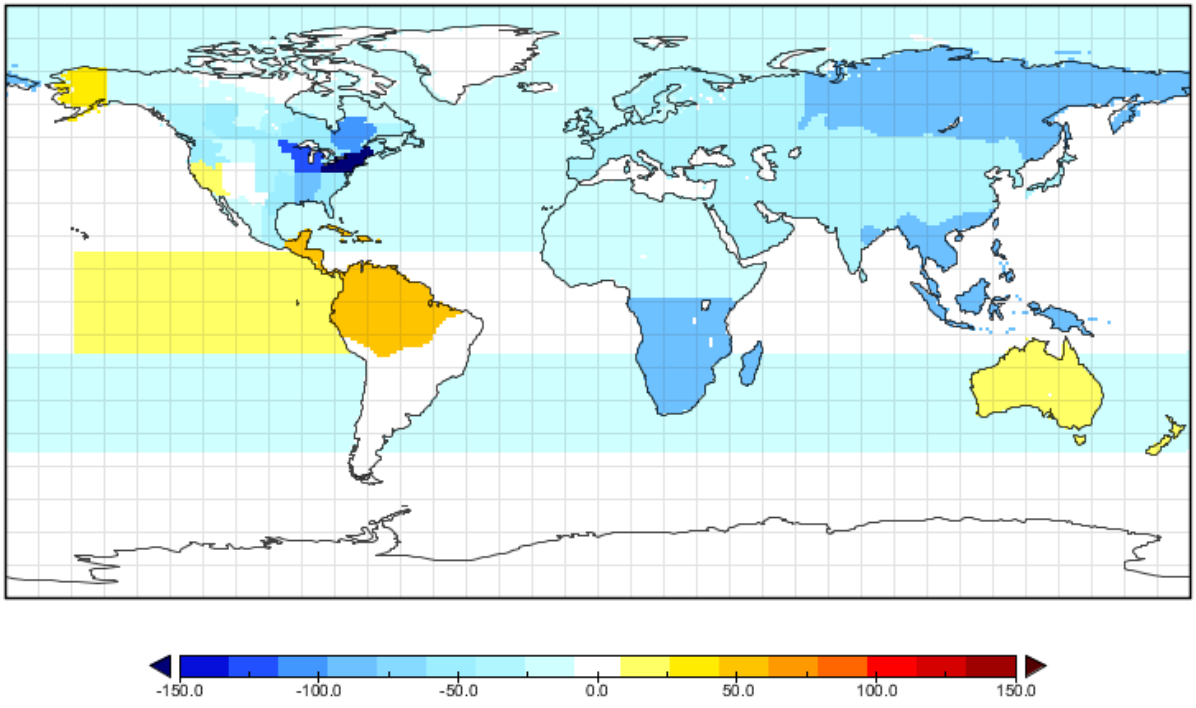

Figure 8. Global distribution of inverted CO_2 flux using CO_2 data only ((gC $m^{-2}y^{-1}$, 2002-2004 average).

Geosci. Model Dev. Discuss., doi:10.5194/gmd-2016-53, 2016
Manuscript under review for journal Geosci. Model Dev.
Published: 17 May 2016

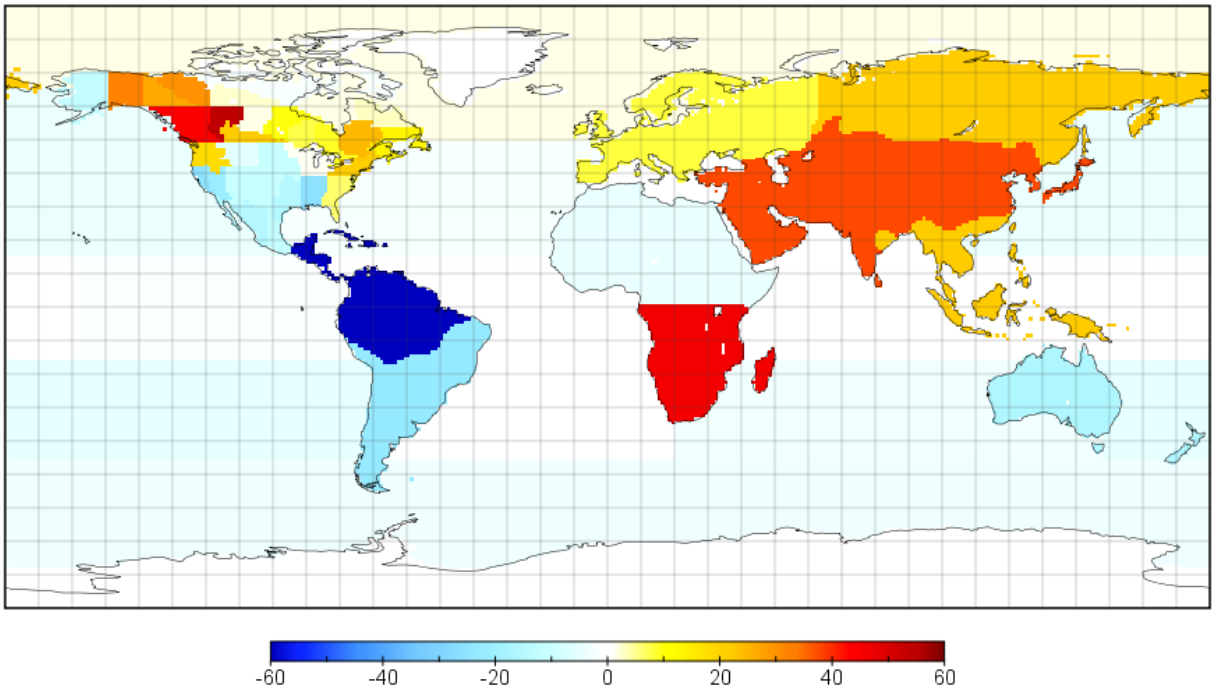

Figure 9. Difference of the inverted CO_2 flux between using CO_2 +$^{13}CO_2$ data and using CO_2 data only (gC $m^{-2}y^{-1}$, 2002-2004 average).

Geosci. Model Dev. Discuss., doi:10.5194/gmd-2016-53, 2016
Manuscript under review for journal Geosci. Model Dev.
Published: 17 May 2016

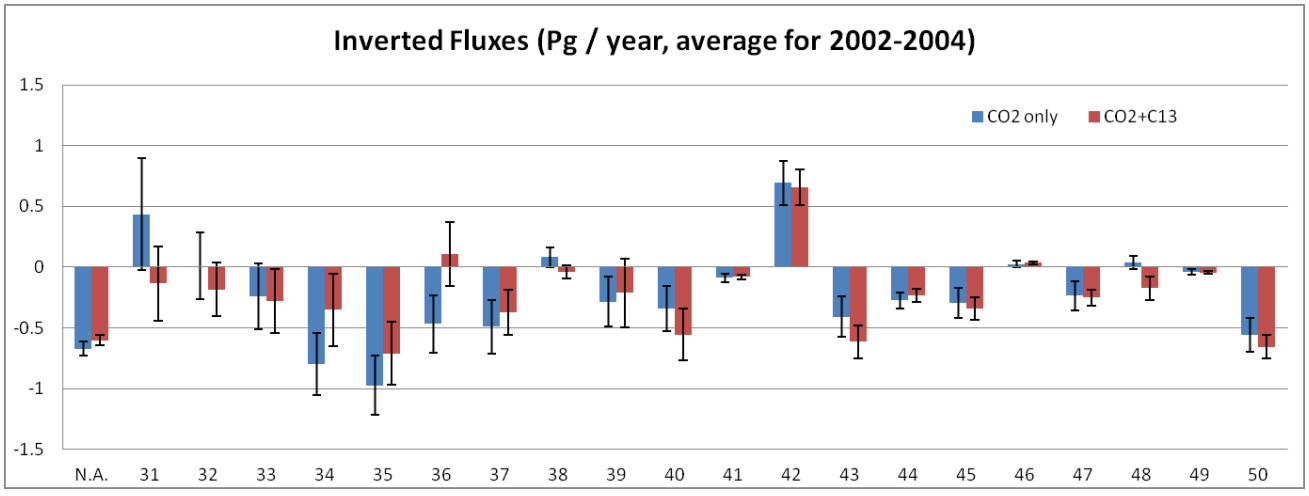

Figure 10. Comparison between inversion results with and without $^{13}CO_2$ constraint for 21 regions of the globe for the periods of 2002-2004.

Geosci. Model Dev. Discuss., doi:10.5194/gmd-2016-53, 2016
Manuscript under review for journal Geosci. Model Dev.
Published: 17 May 2016

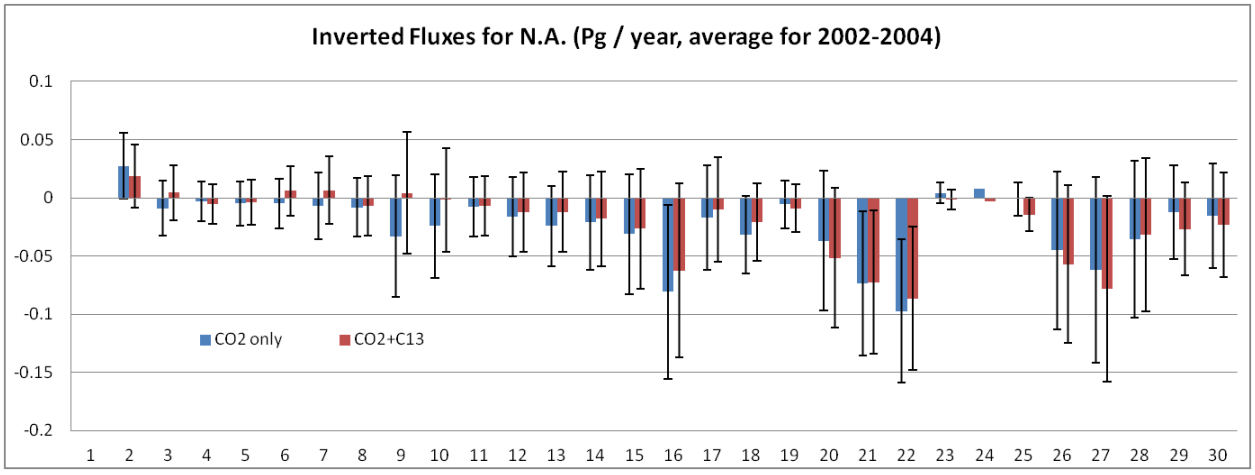

Figure 11. Comparison between inversion results with and without $^{13}CO_2$ constraint for 30 regions in North America.

Geosci. Model Dev. Discuss., doi:10.5194/gmd-2016-53, 2016
Manuscript under review for journal Geosci. Model Dev.
Published: 17 May 2016

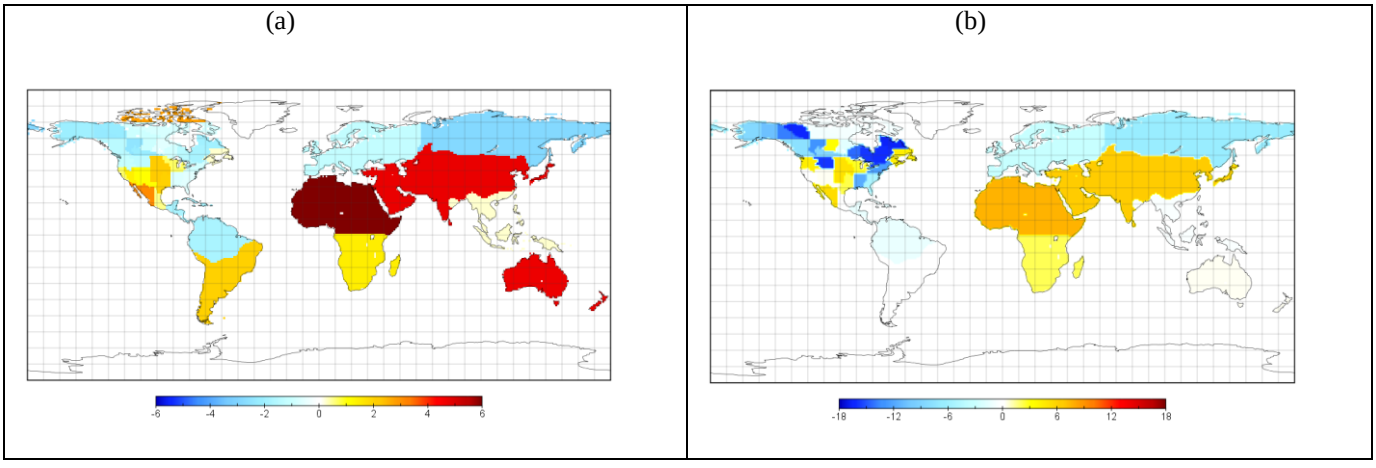

Figure 12. (a) Difference in ε_{lph} (‰) and (b) the inverted CO_2 flux (gC $m^{-2}y^{-1}$) between Case I and Case II, i.e. Case I minus Case II. See Section 2.1.3 for the description of these cases.

Geosci. Model Dev. Discuss., doi:10.5194/gmd-2016-53, 2016
Manuscript under review for journal Geosci. Model Dev.
Published: 17 May 2016

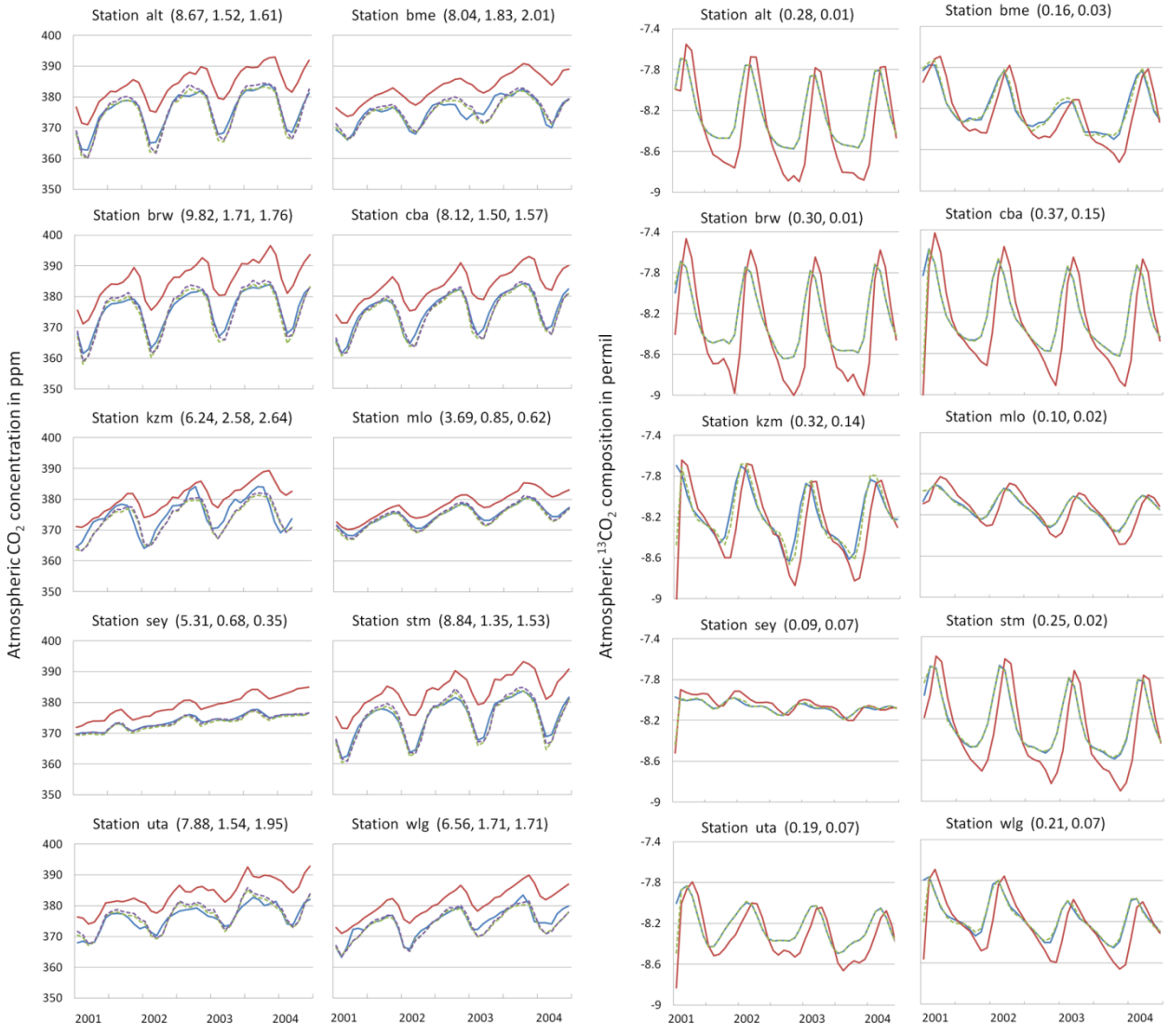

Figure 13. Left panel: comparison of CO_2 concentrations calculated using the prior flux (solid red) and from CO_2-only inversion (dashed purple) and joint inversion (dashed green) against observations (green) at 10 randomly selected stations from different regions. The header of each plot indicates the station ID and the root mean square difference (RMSD) for the prior, joint and CO_2-only inversions against observations. Right panel: comparison of $^{13}CO_2$ composition from the prior (solid red) and joint inversion (dashed purple) against observations (green). The header of each plot indicates the station ID and RMSD of the prior and the joint inversion against observations.

Geosci. Model Dev. Discuss., doi:10.5194/gmd-2016-53, 2016
Manuscript under review for journal Geosci. Model Dev.
Published: 17 May 2016

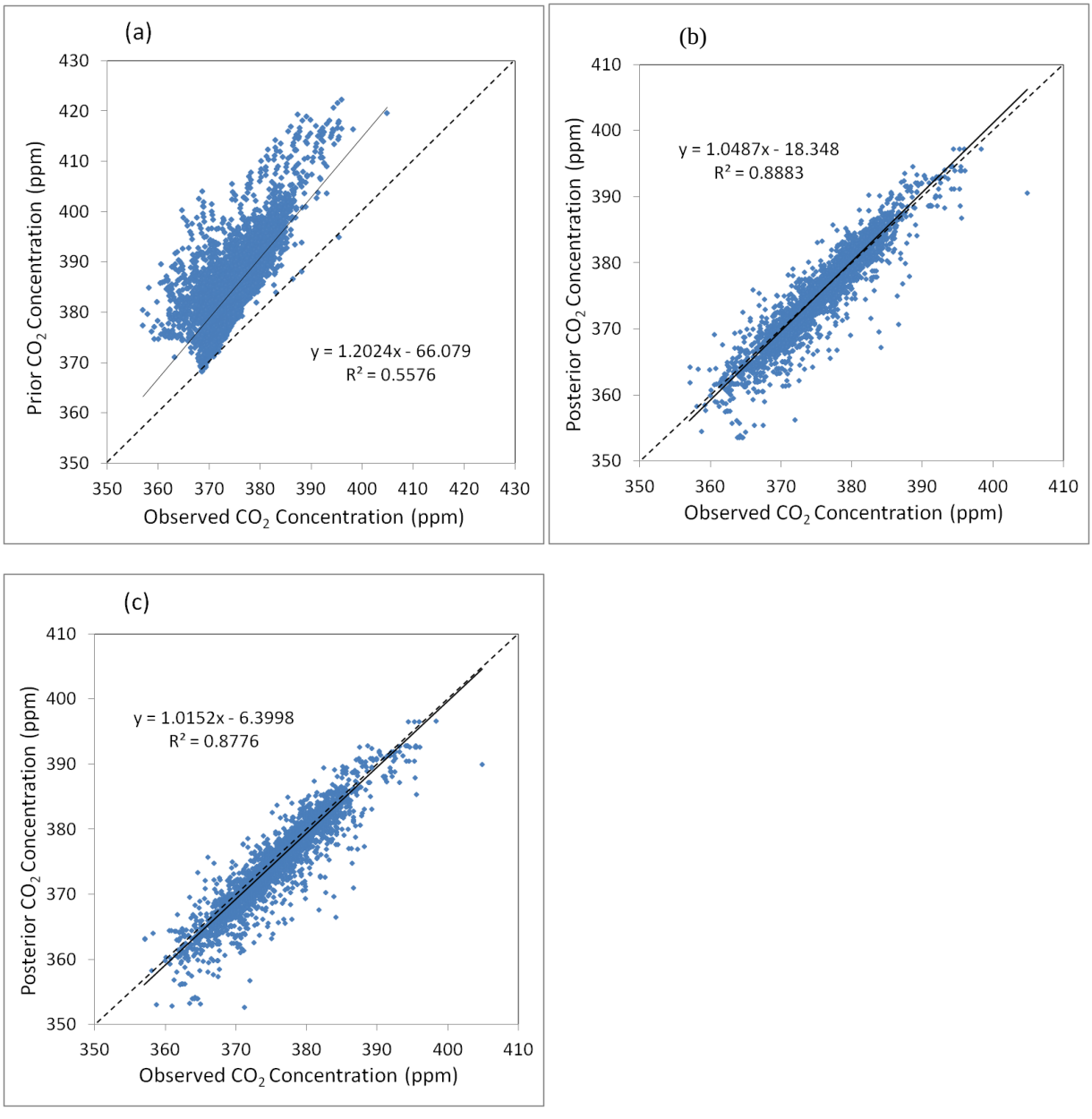

Figure 14. CO_2 concentrations from (a) prior, (b) posterior from the CO_2-only inversion, and (c) posterior from the joint inversion in comparison with observations. The prior concentration is obtained through transport modeling with prior CO_2 fluxes from the terrestrial ecosystems, oceans, fossil fuel emission, and biomass burning.

Geosci. Model Dev. Discuss., doi:10.5194/gmd-2016-53, 2016
Manuscript under review for journal Geosci. Model Dev.
Published: 17 May 2016

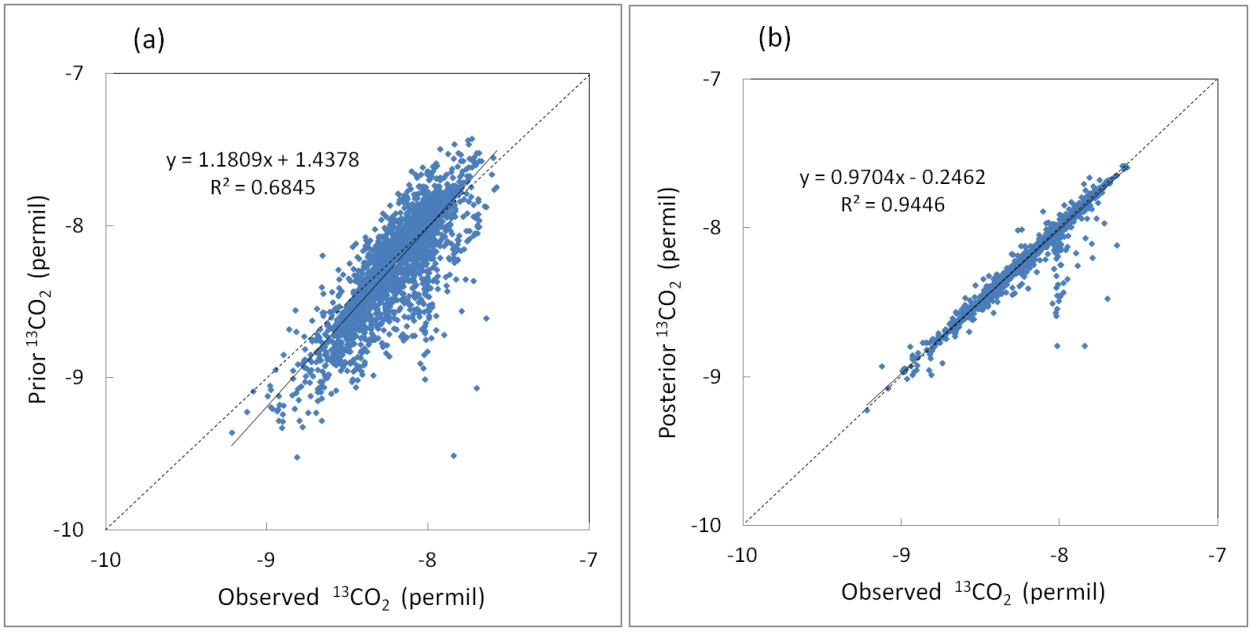

Figure 15. Comparison of prior (a) and posterior (b) $^{13}CO_2$ compositions with observations. The prior composition is obtained through transport modeling with prior $^{13}CO_2$ fluxes from the terrestrial ecosystems, oceans, fossil fuel emission, and biomass burning, and the posterior composition is obtained with the CO_2-$^{13}CO_2$ joint inversion (Case I).